Geochemistry, Geophysics, Geosystems

RESEARCH ARTICLE
10.1029/2018GC007899

Key Points:
- Calculated history of dynamic support of Iberia
- Excess asthenospheric temperatures support up to 1 km of topography
- Marine terraces and geomorphology suggest growth of support in last ∼30 Ma

Correspondence to:
G. G. Roberts,
gareth.roberts@imperial.ac.uk

Citation:
Conway-Jones, B. W., Roberts, G. G., Fichtner, A., & Hoggard, M. (2019). Neogene epeirogeny of Iberia. *Geochemistry, Geophysics, Geosystems*, *20*, 1138–1163. https://doi.org/10.1029/2018GC007899

Received 9 AUG 2018
Accepted 16 JAN 2019
Accepted article online 18 JAN 2019
Published online 25 FEB 2019

Neogene Epeirogeny of Iberia

Benedict W. Conway-Jones[1,2], Gareth G. Roberts[1], Andreas Fichtner[3], and Mark Hoggard[4]

[1]Department of Earth Science and Engineering, Imperial College London, London, UK, [2]Now at Department of Earth Sciences, University of Cambridge, Cambridge, UK, [3]Department of Earth Sciences, ETH Zürich, Zürich, Switzerland, [4]Department of Earth and Planetary Sciences, Harvard University, Cambridge, MA, USA

Abstract The origin of Iberia's topography is examined by combining gravity, magmatic, topographic, and seismological observations with geomorphic considerations. We have four principal results. First, the highest coherence between free-air gravity and topography is at wavelengths $\lesssim$250 km where admittance indicates that elastic thickness of Iberia's plate is 20 ± 3 km. These results imply that flexural and subplate support of Iberian topography could be expressed at wavelengths of O(100) km. Second, P-to-S receiver functions and simple isostatic calculations indicate that while crustal thickness variations and flexural loading (e.g., as a result of plate shortening) partially explain the elevation of Pyrenean, Betics, Cantabrian, Spanish Central System, and Iberian Chain topography, they fail to explain the elevation of large parts of Iberia. Third, a new full waveform shear wave tomographic model and velocity to temperature conversions suggest that the asthenosphere beneath Iberia is anomalously slow and has excess temperatures of up to 162 ± 14 °C. Simple isostatic calculations indicate asthenospheric support of topography of up to 1 km. Neogene-Recent (∼23–0 Ma) extrusive magmatism (e.g., Calatrava, Catalan) sit atop many of the slow shear wave velocity anomalies. Finally, biostratigraphic data, combined with inversion of 3,217 river profiles, show that most of Iberia's topography grew during the last ∼30 Ma at rates of up to 0.3 mm/year. Best-fitting theoretical rivers have a low residual root-mean-square misfit (= 0.96) and calculated uplift is consistent with an independent inventory of stratigraphic and biostratigraphic observations. We suggest that Neogene-Recent growth of most of central Iberia's topography was a result of asthenospheric support.

1. Introduction

Histories of uplift in dynamically supported regions contain clues about spatial and temporal evolution of mantle convection. Here we focus on Iberia where, away from its highest mountains, kilometer-scale topography does not appear to be supported solely by crustal isostasy.

Our approach to calculating the history of subplate support beneath Iberia and its uplift history has three steps. First, we examine the isostatic contributions to modern topography from crustal thicknesses. Admittance between gravity and topography is calculated to estimate the elastic thickness of Iberia's plate and used to examine wavelengths at which lithospheric loading and flexure are important. Second, biostratigraphic and cosmogenic dating of uplifted marine terraces are combined with calibrated inversion of Iberia's drainage patterns to investigate its Neogene history of uplift. Finally, a new full waveform shear wave tomographic model is converted to temperature and used to estimate excess mantle temperatures, which are combined with simple isostatic calculations to estimate the role asthenospheric temperatures play in supporting Iberian topography.

1.1. Lithospheric Structure and Isostasy

Topographic evolution of Iberia has largely been attributed to crustal thickening and by some to lithospheric-scale buckling (e.g., Cloetingh et al., 2002; Muñoz-Martín et al., 2010). There have been recent significant advances in our understanding of the crustal, lithospheric, and subplate structure beneath Iberia and its surroundings from seismology. Importantly, a dense (∼60 × 60 km) grid of broadband seismometers was deployed across the peninsula between 2007 and 2013 as part of the TopoIberia – IberArray experiment (see, e.g., Palomeras et al., 2017). Data from this experiment and others have been used to calculate crustal thicknesses from receiver functions, Rayleigh wave tomography, and to derive a full waveform shear wave model of lithospheric and sublithospheric structure (Fichtner & Villaseñor, 2015; Mancilla & Diaz, 2015; Palomeras et al., 2017). The full waveform model has been updated in this study.

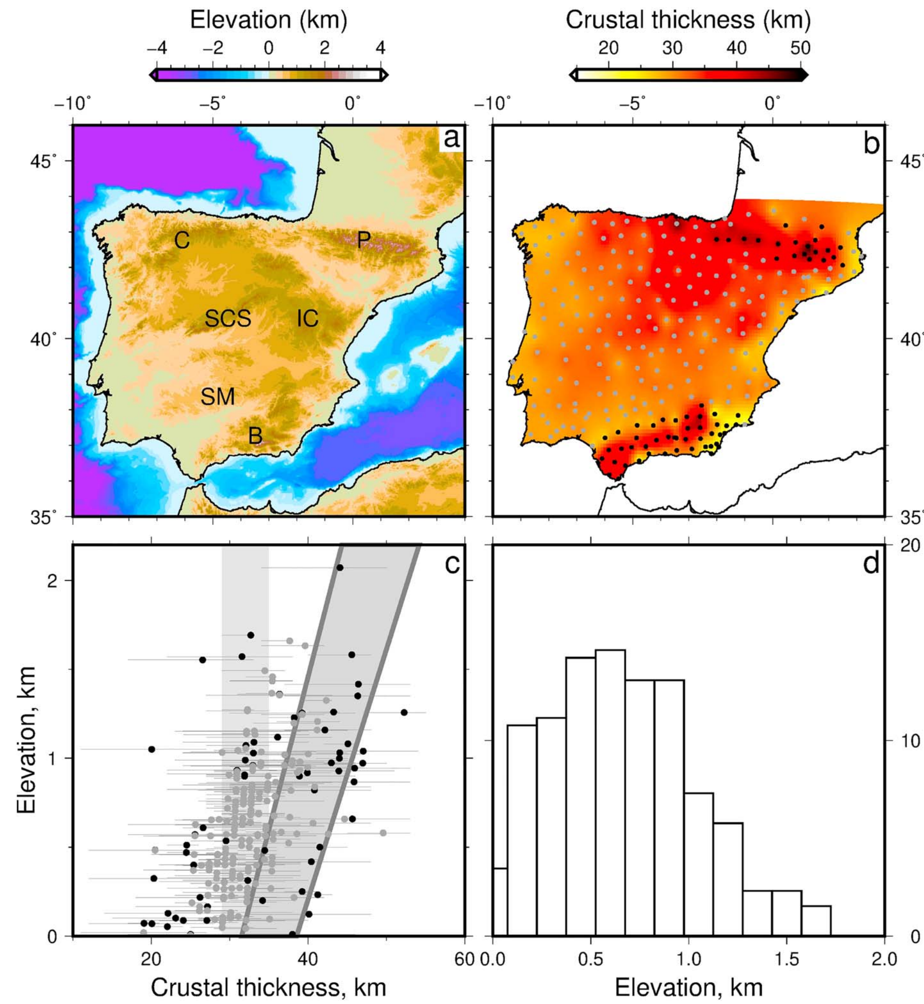

Figure 1. Topography and crustal thickness. (a) Iberian topography from ASTERGDEM and ETOPO1. P = Pyrenees; C = Cantabrian Mountains; SCS = Spanish Central System; IC = Iberian Chain; SM = Sierra Morena; B = Betics. (b) Color scale = crustal thicknesses interpolated using splines between measurements from receiver function H–κ stacking analyses (circles; Mancilla & Diaz, 2015). (c) Gray/black circles = elevation versus crustal thickness. Black circles = crustal thickness estimates from the Pyrenees and Betics (see panels (a) and (b)). Gray rectangular envelope = crustal thicknesses of 32 ± 3 km. Gray polygon = relationship between crustal thickness, t_c, and elevation, e, which is calculated by equalizing pressure at base of continental lithosphere against a mid-oceanic ridge such that $e\rho_a = t_w(\rho_w - \rho_a) + t_{oc}(\rho_{oc} - \rho_a) + t_m(\rho_a - \rho_m) - t_c(\rho_c - \rho_a)$, where water depth $t_w = 2.5$ km, density $\rho_w = 1{,}000$ kg/m^3, crustal thickness $t_{oc} = 7.1$ km, density $\rho_{oc} = 2{,}800$ kg/m^3, asthenospheric density $\rho_a = 3{,}200$ kg/m^3, lithospheric mantle thickness $t_m = 90$ km, and density, $\rho_m = 3{,}300$ kg/m^3. Width of envelope shows calculated elevations for range of continental crustal densities ($\rho_c = 2{,}700 \pm 50$ kg/m^3). Note most central Iberian crustal thickness estimates lie within 32 ± 3 km and are generally not consistent with this simple isostatic model. (d) Histogram of Iberian topography, y axes = percentage; note broad peak centered at ~0.6 km.

Figure 1 summarizes Mancilla and Diaz (2015)'s crustal thickness (H) and Vp/Vs (κ) ratios calculated using H–κ stacking of P-to-S receiver functions from >300 stations, including IberArray, across Iberia and its surroundings. Many of their best constrained estimates (reported errors of ±2 km) are in the western half of Iberia, where calculated crustal thicknesses are 25–35 km and Vp/Vs ratios are 1.72–1.75. Two regions centered on the Central System and the Iberian Chain have calculated thicknesses up to 40–45 km. The Pyrenean range and the Betic mountains have the highest calculated thicknesses, which are in excess of 45 ± 8 km in places. These values are consistent with a suite of wide-angle/refraction experiments and recent Rayleigh wave tomography (see Díaz & Gallart, 2009; Palomeras et al., 2017). Large portions of the central Iberian plateau have crustal thicknesses of 35 km or less and no clear correlation with elevation (Figure 1c; Mancilla & Diaz, 2015).

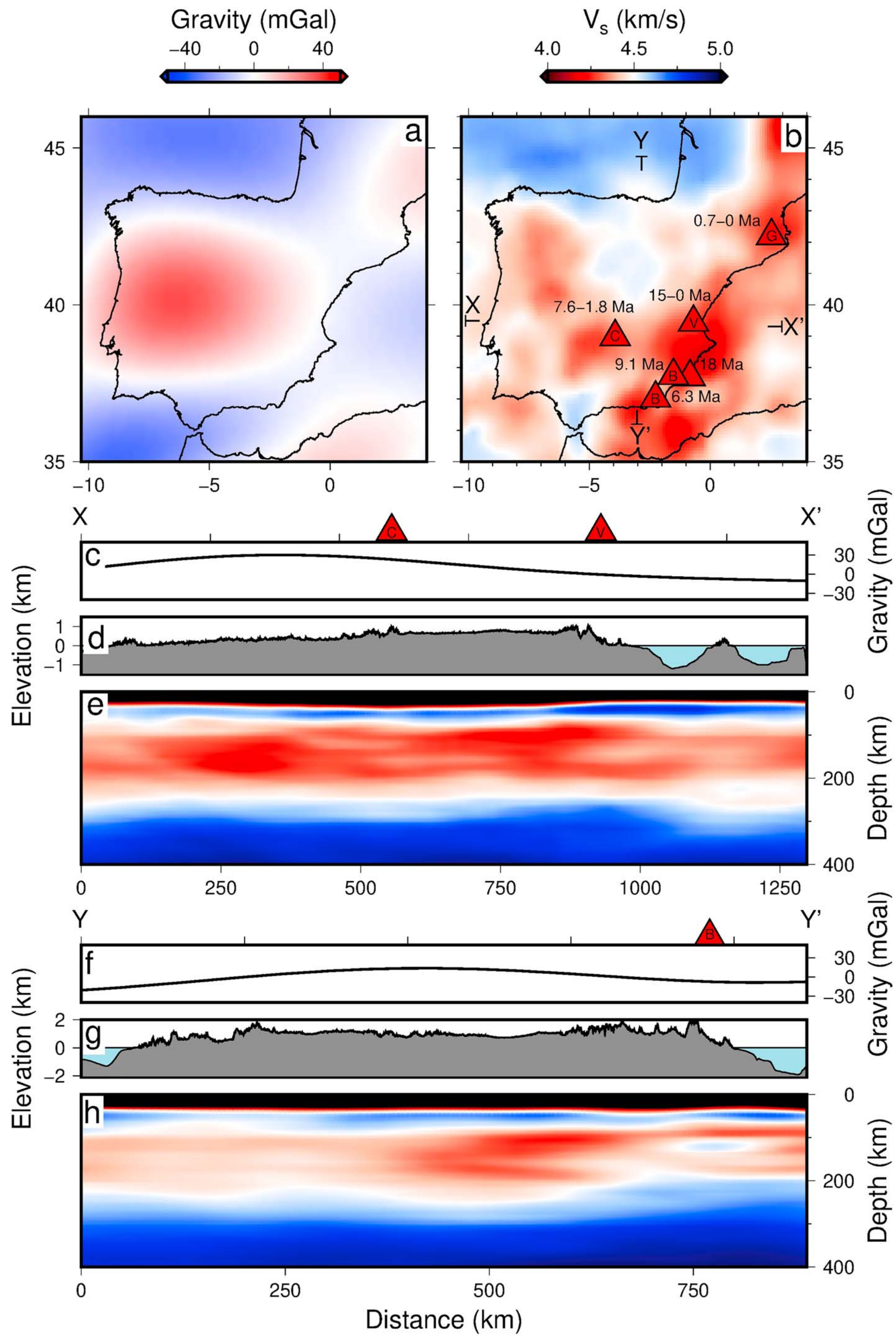

Figure 2. Gravity, magmatism, and shear wave tomography. (a) GRACE free-air gravity data band-pass filtered between wavelengths of 730 and 9,000 km (Tapley et al., 2007). (b) Full waveform shear wave tomographic model at 90 km depth (updated from ; Fichtner & Villaseñor, 2015). Labels X, X′, Y, and Y′ = transects shown in panels (c)–(h). Red labeled triangles = magmatic provinces: G = Garrotxa, Catalan Volcanic zone, 700–11 kyr, K-Ar dating (Cebriá et al., 2000); V = Valencia volcanic zone, 15–0 Ma, K-Ar dating (Martí et al., 1992); C = Calatrava, 7.6–1.75 Ma, K-Ar dating (Cebriá & Lopez-Ruiz, 1995); B = Betics, from east to west: Mar Menor (~18 Ma), Mazarron (~9.1 Ma), and El Hoyazo (~6.3 Ma), all U-Th-Pb dating (Alvarez-Valero & Kriegsman, 2007). (c and f) GRACE free-air gravity data along X-X′ and Y-Y′ transects (Tapley et al., 2007). Locations of Calatrava, Valencia, and Betic volcanic zones are shown as red triangles. (d and g) ASTERGEM elevation and ETOPO1 bathymetry along X-X′ and Y-Y′ transects, respectively. (e and h) Cross sections through full waveform tomographic model. Black polygons = velocities, $V_s \leq 4.0$ km/s. Note slow velocities ($V_s < 4.4$ km/s) between ~ 50 and 250 km depth beneath Calatrava and Valencia volcanic regions.

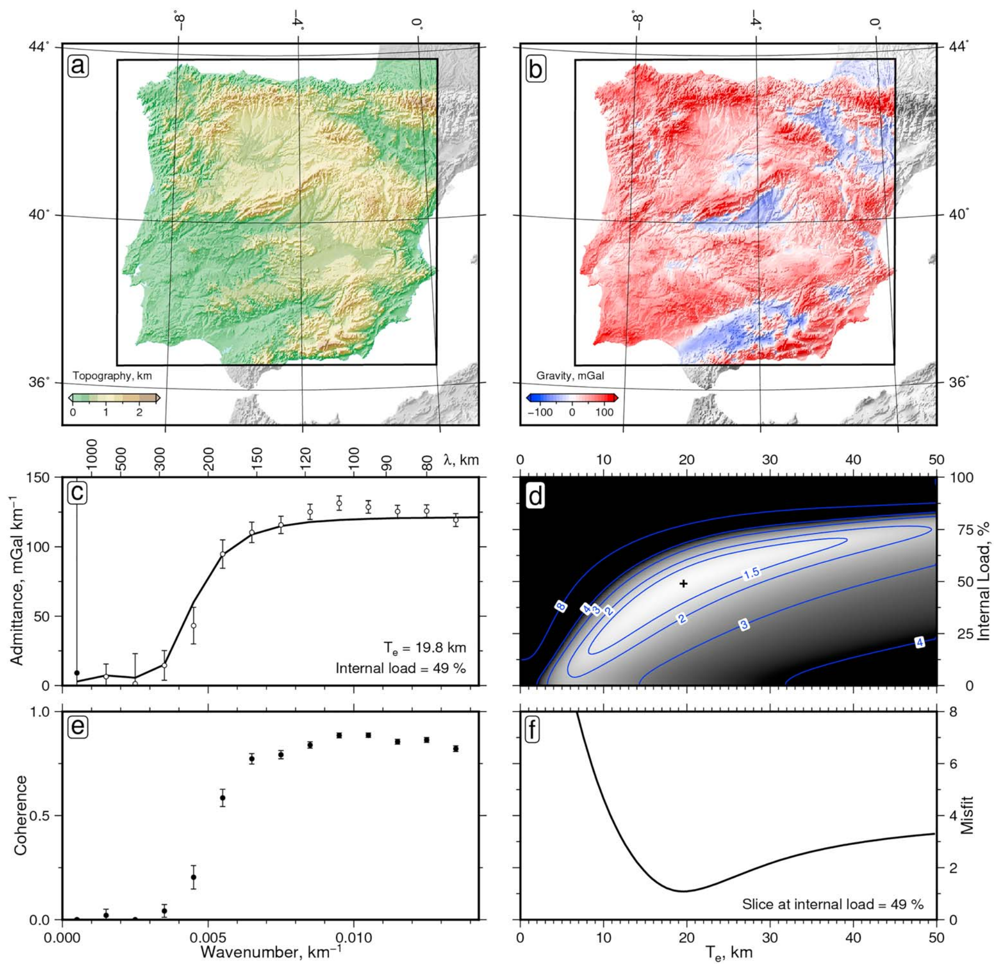

Figure 3. Admittance between gravity and topography.(a) Topography from SRTM30_plus (Becker et al., 2009); box encloses region used in analysis. (b) EIGEN – 6C3stat free-air gravity anomalies (Förste et al., 2012). (c) Admittance and standard deviation as a function of wave number (i.e., $k = \lambda^{-1}$, where λ = wavelength) for coherent component of gravity anomalies. Black line = best-fitting elastic model with T_e = 19.8 km and coherent internal load, F_2 = 49% (other parameters given in main text); open circles = values used to constrain misfit. (d) Misfit as a function of T_e and F_2; cross = minimum. (e) Coherence as a function of wave number. Note high coherence for $\lambda < 200$ km. (f) Slice through misfit function at best fit F_2 = 49%.

Simple isostatic calculations indicate that most of central Iberia should sit close to or below sea level (Figure 1c; e.g., Roberts, White, et al., 2012). Instead, it has an average elevation of +0.6 km (Figure 1d). One way to solve this problem is to invoke anomalously low crustal densities. However, crustal velocities estimated from wide-angle seismic experiments suggest that the crust beneath Iberia is not of especially low density. For example, Díaz and Gallart (2009) show that crustal velocities in the western and central parts of the peninsula are 5.9–6.1 km/s at depths $\lesssim$10 km, 6.2–6.4 km/s at depths ~10–20 km, and 6.7–6.8 km/s at depths $\gtrsim$20 km, which implies densities, $\rho \approx 2{,}800 \pm 400$ kg/m^3 (e.g., Barton & Wood, 1984). These observations and simple calculations suggest that the mantle might play an important role in supporting Iberian topography (cf. Fernandez et al., 1998). We examine the contribution from the mantle using a suite of long wavelength geophysical observations and the magmatic history of the peninsula.

1.2. Subplate Support and Magmatism

Free-air gravity anomalies, band-pass filtered to wavelengths ~730–9,000 km, exhibit a +30 mGal peak that encompasses most of western and central Iberia (e.g., Figure 2a; Tapley et al., 2007). This positive gravity anomaly indicates that not all Iberian topography is caused by simple crustal isostasy (e.g., Colli et al., 2016; McKenzie, 2010). The ratio (i.e., admittance, Z) between coherent free-air gravity anomalies and topography as a function of wave number, k, can be used to investigate dynamic support, internal loading, and the elastic

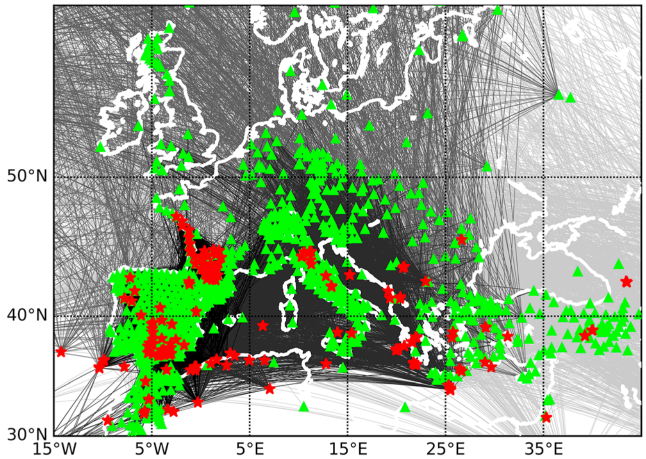

Figure 4. Seismic data coverage. Stars/triangles = sources/receivers used to generate the shear wave tomographic model (e.g., Figure 2). Thin lines = great-circle ray paths of the data. White = coastlines.

thickness of the plate. Admittance is calculated such that

$$Z(k) = \frac{< gt^* >}{< tt^* >}, \tag{1}$$

where g and t are multitaper Fourier transforms of free-air gravity and topography data averaged over wave number bands, with complex conjugates denoted by asterisks (McKenzie & Fairhead, 1997). Figure 3 shows the admittance between SRTM30_plus topography and EIGEN-6C3stat gravity data sets (Becker et al., 2009; Förste et al., 2012). Unfortunately, low coherence between Iberian topography and gravity at long wavelengths (>300 km) means that the value of admittance and, for example, an inferred amplitude of dynamic support is poorly constrained (Figure 3e). However, coherence is sufficiently high for wavelengths <250 km that the elastic thickness, T_e, of the plate can be investigated.

T_e is estimated by comparing the observed values of $Z(k)$ with a theoretical curve generated using a two-layer crustal model overlying a mantle half-space (McKenzie, 2003). Upper crustal density controls the magnitude of admittance at the shortest wavelengths. We adopt a crustal template consisting of a 10-km upper crust with density of 2,900 kg/m^3 and a 25-km lower crust with density of 3,000 kg/m^3. A parameter sweep is carried out where T_e and the fraction of internal loading that is coherent with the topography, F_2, are systematically varied, and misfit to observed admittance is calculated (Figure 3d). The best-fitting model has $T_e = 19.8 \pm 3$ km and an internal load of 49%, which is broadly consistent with results of flexural modeling in the Ebro basin and central Iberian Peninsula (Gaspar-Escribano et al., 2001; Ruiz et al., 2006). These results suggest that the plate's flexural response to loads should be confined to wavelengths of O(100) km. Negative free-air gravity anomalies that extend up to ~200 km from the northern and southern fringes of the Spanish Central System, in the Ebro basin, and north of the Betic Cordillera are probably partially generated by the flexural response of the lithosphere to loading induced by shortening (Figure 3a; e.g., Banks & Warburton, 1991; Muñoz, 1992; Vissers et al., 1995). Backstripped subsidence curves from these basins indicate that they experienced local Cenozoic tectonic subsidence in excess of a few hundred meters (see, e.g., De Vicente et al., 2011, and references therein). A corollary is that the flexural effects of loading cannot explain the elevation of Iberia's longer wavelength low-relief topography.

We examine the structure of the crust and mantle beneath Iberia using the shear wave tomographic model shown in Figure 2. This model is the result of successive refinements at increasingly higher frequencies, comprising, in this order, Europe as a whole, the western Mediterranean, and the Iberian Peninsula. The last stage, which is an improvement of the model by Fichtner and Villaseñor (2015), is based on ambient noise correlations at a minimum period of 5 s. As a result of the multiscale inversion, the total frequency bandwidth for the Iberian Peninsula is 5–120 s. This bandwidth combined with the exploitation of complete seismograms, including three-component body and surface waves, allows us to jointly constrain crustal and mantle structure. The full-waveform inversion does not require crustal corrections and therefore avoids artifacts in upper mantle structure that may result from an imperfect crustal model (Bozdag & Trampert, 2008).

The sequence of multiscale refinements involves 131 earthquakes and 81 virtual sources from noise correlations. These events provide a total of 34,184 three-component waveform recordings, with particularly dense coverage around the IberArray installation (Díaz et al., 2009; Figure 4). Thanks to this dense coverage, tomographic resolution beneath the Iberian Peninsula is mostly controlled by the minimum period of the seismic waves probing a specific part of Earth structure. Within the upper mantle, mostly constrained by surface waves at periods around 20 s, horizontal and vertical resolution lengths are generally below 100 and 50 km, respectively, which is confirmed by quantitative resolution analysis (Fichtner & van Leeuwen, 2015). An east-west cross section through the full waveform model shows that central Iberia has relatively slow seismic velocities (<4.4 km/s) between 0 and 300 km depth (Figures 2c–2e). These results are broadly consistent with independent Rayleigh wave tomography (Palomeras et al., 2017). A north-south transect displays a low velocity zone beneath central Iberia, coinciding with low-relief, long wavelength, topography, and crust ~5 km thinner than areas outside this region (Figures 2f–2h; cf. Quintana et al., 2015).

10.1029/2018GC007899

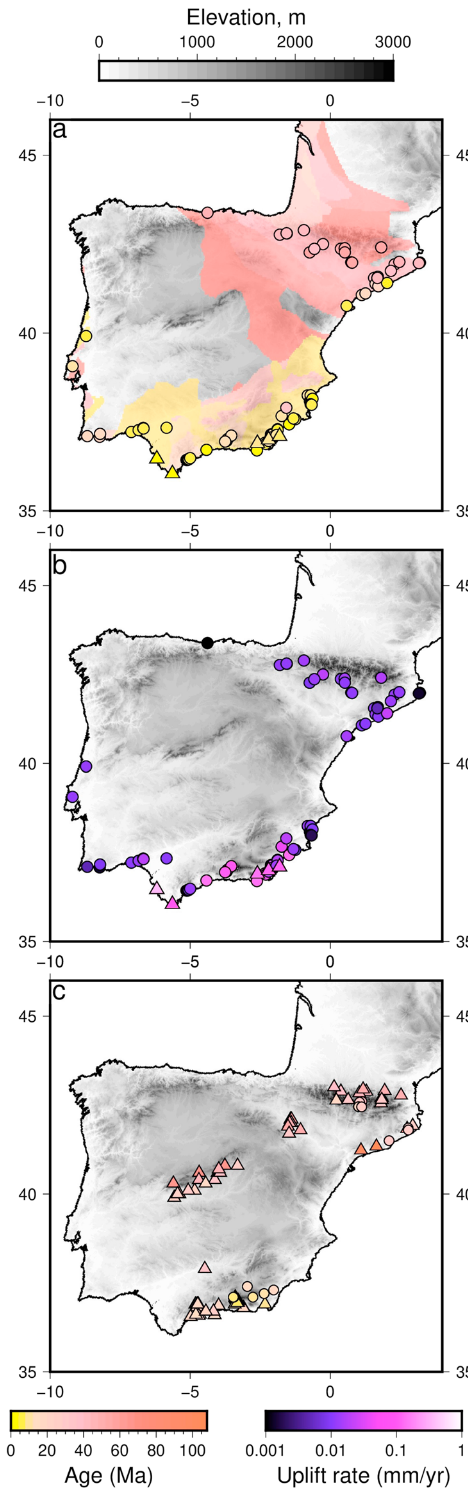

Figure 5. Uplift history from biostratigraphic data. (a) Grayscale = shaded topography from ASTER GDEM. Colored swatches = youngest marine and coastal stratigraphy (e.g., Alonso et al., 1993; Braga et al., 2003; Pomar et al., 2017). Circles = Cenozoic marine fossils recorded in the PaleoDB inventory colored by age (Table 1). Triangles = radiometric dating of marine terraces (e.g., Benedetti et al., 2009; Braga et al., 2003; Gracia et al., 2008; Zazo et al., 1999, 2003). (b) Circles/triangles are colored by average uplift rates calculated using the age and elevation of marine rock (see body text and Table 1). (c) Thermochronmetic closure ages. Triangles and circles = apatite fission track and (U-Th)/He derived ages, respectively (see body text; Andriessen & Zeck, 1996; de Bruijne & Andriessen, 2002; Del Río et al., 2009; J. J. Esteban et al., 2004; Fitzgerald et al., 1999; Gibson et al., 2007; Johnson, 1997; Juez-Larré & Andriessen, 2006; Lonergan & Johnson, 1998; Morris et al., 1998; Platt et al., 2003, 2005; Vázquez et al., 2011).

Neogene-Recent magmatism in central, southern, and north eastern Iberia sit atop loci of slow upper mantle shear wave velocities (Figure 2b). For example, K-Ar dated Miocene leucitites and Pliocene basalts crop out in the Calatrava Volcanic Province, and their major, trace, and isotope chemistry suggest that the asthenosphere has become an increasingly important source of magmatism (Cebriá & Lopez-Ruiz, 1995). A similar trend is observed in southern Iberia where $^{40}Ar/^{39}Ar$ dated Late Miocene Si-K-rich rocks are found in close proximity to Pleistocene Si-poor, Na-rich compositions (Duggen et al., 2005). These observations have been interpreted as a transition from subduction-related magmatism to melting with an asthenospheric source and have been related to kilometer-scale uplift of Iberia's southern margin (Duggen et al., 2004). Similarly, Quaternary magmatism in the Catalan Volcanic Province, northeastern Iberia, probably had a significant contribution from asthenospheric sources (Cebriá et al., 2000). These observations indicate that mantle beneath Iberia is anomalously warm (cf. Carballo et al., 2015).

To better understand the history of subplate processes we examine the evolution of Iberian topography in space and time by combining stratigraphic observations with magmatic and geomorphic data and theory.

2. A History of Vertical Motions

2.1. Stratigraphic Constraints

Uplift histories at spot locations across Iberia have been constrained using the distribution of Cenozoic marine sedimentary rock (e.g., M. Esteban, 1996; Janssen et al., 1993; Figure 5 and Table 1). Shallow marine Paleocene sedimentation in north, east, and southern Iberia indicate that at ~65–60 Ma large parts of Iberia were low-lying (Andeweg, 2002). The distribution of planktonic formaminiferal marls (e.g., Tubilla del Agua fm.), sabkha deposits (e.g., Santo Domingo de Silos fm.), and temporary intertidal zones (e.g., Sierra Perenchiza) were probably formed as a result of fluctuating sea level and flooding of low-relief topography (Alonso et al., 1993).

In the Ebro basin, eastern Iberia, coral reefs (e.g., the Buil Level within the Barranco El Solano sequence and mounds within the Guara formation) indicate extensive Paleogene reef building and mesophotic zone carbonate platform production (Pomar et al., 2017). Reef building appears to have moved eastward through time, from Merli (56–48 Ma) to the Meson de Ligüerre reefs (47–42 Ma; Pomar et al., 2017). The Cardona Salt, which crops out within the basin, indicates a Priabonian (~37 Ma) transition from marine to continental deposition (Vergés et al., 1995). Oligocene continental sediments in eastern parts of the Ebro basin contain micromammal fossils (e.g., *Theridomys aff. aquatilis* Aymard within the red bed sequence of the Artes formation), which suggest that by ~30 Ma most of eastern Iberia was emergent probably as a result of plate shortening (Agustí et al., 1987; Vergés et al., 1995). Stratigraphy of the lower Tagus basin (e.g., Musgueira Limestones with *Chlamys scabriuscula*) indicate Miocene-Recent emergence of parts of western Iberia (Andeweg, 2002; Geel et al., 1992; Pais, 2004; Pais et al., 2012). These results are corroborated by commercial well logs, which suggest that the Porto Basin contains Paleogene marine facies (Murillas et al., 1990).

Uplift is best constrained along the southern coast and in particular across the Betic Cordillera. During the Serravallian (13.6–11.6 Ma) the cordillera began to emerge as reef-bound islands (Braga et al., 2003; Geel et al., 1992). Uplifted corals (e.g., *Porites*; *Tarbellastrea*), marine bivalves (e.g., *Pecten*; *Crassostrea gryphoides*), and planktonic foraminifera (e.g., *Globorotalia suterae*) indicate that prior to ~7 Ma a ~10 km wide seaway connected the Atlantic Ocean to the Mediterranean Sea through the Guadix basin in southern Iberia (Betzler et al., 2006). The elevation of outcropping marine fauna suggests average rates of uplift in southern Iberia of up to 0.3 mm/year during the last ~15 Ma (e.g., Braga et al., 2003). Marine sedimentation in the Poniente, Almería-Níjar, and Vera basins indicate that Almería to Sorbas was marine as recently as 3 Ma (Braga et al., 2003). In summary, a suite of stratigraphic observations show that most of Iberia underwent significant, O(100–1,000) m, Cenozoic uplift.

2.2. Biostratigraphic Database

As an adjunct to this compilation of uplift constraints, we have used Cenozoic marine fossils recorded in the Paleobiological Database and radiometrically dated marine terraces to estimate uplift of Iberia (PaleoDB: `https://paleobiodb.org`; Figure 5). Most of the PaleoDB samples are concentrated along the southern coast and in the Pyrenean mountains. The database of samples from the Pyrenees is rich in Paleogene marine fossils and generally lacks marine fossils younger than ~35 Ma. In contrast, the majority of marine samples from Iberia's southern coast are Neogene in age, and few specimens have ages older than 17 Ma

Table 1
Observed Uplift Rates From Dated Fossil (F), Marine Terrace (M), and Sediment Deposit (S) Studies (See Figure 5)

Lat	Long	Method	Fossil (e.g.)	Age (Ma)	PWD (m)	H (m)	Uplift rate	Study
38.00	−0.70	F	Lithothamnion sp.	4.47 ± 0.5	2.5 ± 2.5	10	0.003 ± 0.0008	Braga 2001
37.98	−0.67	F	Pectinidae indet.	4.47 ± 0.5	2.5 ± 2.5	13	0.003 ± 0.0009	Braga 2001
41.55	1.69	F	Placosmiliopsis bilobatus	39.7 ± 1.65	5 ± 5	279	0.007 ± 0.0004	Pérez 2012
37.17	−8.22	F	Erylus sp.	12.7 ± 1.10	60 ± 20	64	0.01 ± 0.002	Pisera 2006
37.34	−5.84	F	Balaenopteridae indet.	4.47 ± 0.87	2.5 ± 2.5	58	0.014 ± 0.003	Sendra 1996
39.92	−8.72	F	Favartia sp., Persicula sp.	3.96 ± 0.37	10 ± 10	57	0.017 ± 0.004	Da Silva 2010
42.00	2.47	F	Nummulites verneuili	44.6 ± 3.25	5 ± 5	733	0.017 ± 0.001	Serra 2003
37.60	−1.31	F	Metaxytherium	3.96 ± 0.37	10 ± 10	71	0.02 ± 0.004	Sorbi 2012
42.37	−0.57	F	Actinacis sp.	36.0 ± 2.05	10 ± 10	724	0.02 ± 0.001	Morsilli 2012
41.75	2.17	F	Bryozoa indet.	36.0 ± 2.05	20 ± 20	699	0.02 ± 0.002	Taberner 1995
37.13	−1.92	F	Mesophyllum sp.	7.60 ± 1.70	5 ± 5	180	$0.024 \pm^{0.007}_{0.004}$	Braga 2001
37.90	−1.57	F	Archaias sp.	31.0 ± 2.90	2.5 ± 2.5	1,104	$0.036 \pm^{0.043}_{0.020}$	Braga 2011
37.05	−2.13	F	Halimeda sp.	6.29 ± 0.96	20 ± 5	497	$0.082 \pm^{0.005}_{0.06}$	Braga 2009
37.15	−2.12	F	Porites sp.	6.29 ± 0.96	25 ± 25	524	$0.087 \pm^{0.019}_{0.014}$	D'Estevou 1978
36.95	−3.75	F	Tarbellastraea sp.	9.43 ± 2.19	10 ± 10	1,273	$0.136 \pm^{0.042}_{0.027}$	Braga 1990
37.1	−1.81	S	-	7.5	-	1,387	0.18 ± 0.005	Braga 2003
36.9	−2.60	S	-	7.5	-	2,126	$0.28 \pm^{0.005}_{0.06}$	Braga 2003
43.38	−4.38	F	Alveolinidae indet.	45.0 ± 11.05	5 ± 5	29	0.0007 ± 0.0002	Aguirre 2011
37.08	−8.23	F	Bivalvia indet.	16.0 ± 4.41	25 ± 25	10	$0.002 \pm^{0.003}_{0.0017}$	Forst 2000
43.30	−2.26	F	Oolina sp.	57.6 ± 1.60	225 ± 75	30	0.004 ± 0.001	(Wiedmann, 1960)
43.30	−2.26	F	Stensioeina beccariiformis	57.6 ± 1.60	225 ± 75	30	0.004 ± 0.001	(Wiedmann, 1960)
37.10	−8.67	F	Cetacea indet.	12.7 ± 1.10	75 ± 25	14	0.007 ± 0.002	(Estevens, 2000)
38.09	−0.72	F	Odontoceti indet.	2.67 ± 2.66	10 ± 10	14	$0.009 \pm^{3.391}_{0.006}$	Sendra 1995
38.15	−0.63	F	Ostrea sp., Balanus sp.	1.30 ± 1.29	5 ± 5	8	$0.01 \pm^{1.79}_{0.007}$	Zazo 2003
41.07	1.13	F	Cetacea indet.	13.8 ± 2.18	125 ± 75	14	0.01 ± 0.007	Belaústegui 2011
37.58	−1.25	F	Alca sp.	3.96 ± 0.37	30 ± 30	12	0.011 ± 0.008	(Sanchez-Marco, 2003)
38.09	−0.68	F	Cetacea indet.	1.69 ± 0.90	5 ± 5	16	$0.012 \pm^{0.020}_{0.006}$	Redaccion 2001
41.11	1.26	F	Mysticeti indet.	13.8 ± 2.18	160 ± 40	5	0.012 ± 0.005	Belaústegui 2011
41.32	1.72	F	Tarbellastraea reussiana	17.1 ± 3.31	25 ± 25	184	0.012 ± 0.004	(Chevalier, 1961)
37.22	−7.10	F	Isurus sp.	4.47 ± 0.87	50 ± 50	8	$0.013 \pm^{0.017}_{0.011}$	García 2009
36.43	−5.13	F	Gibbula sp., Atlanta sp.	3.09 ± 0.51	25 ± 25	19	0.014 ± 0.009	Francisco 1993
36.43	−5.10	F	Barbatia barbata	3.96 ± 0.37	50 ± 50	7	$0.014 \pm^{0.015}_{0.012}$	Francisco 1993
38.25	−0.70	F	Porites sp.	6.29 ± 0.96	20 ± 20	61	0.014 ± 0.007	Braga 1995
41.58	1.70	F	Stylocoenia n. sp. aurelii	39.7 ± 1.65	25 ± 25	519	0.014 ± 0.001	Pérez 2012
42.37	0.38	F	Pyrazopsis polygonum	51.9 ± 4.10	5 ± 5	703	0.014 ± 0.001	Dominici 2014
36.45	−5.05	F	Glycymeris glycymeris	3.96 ± 0.37	50 ± 50	8	$0.015 \pm^{0.015}_{0.012}$	Francisco 1993
36.45	−5.08	F	Barbatia barbata	4.47 ± 0.87	50 ± 50	16	$0.015 \pm^{0.017}_{0.011}$	Francisco 1993
41.99	0.75	F	Vicinocerithium	51.9 ± 4.10	5 ± 5	778	0.015 ± 0.001	Dominici 2014
41.98	0.78	F	Vicinocerithium	51.9 ± 4.10	5 ± 5	780	0.015 ± 0.001	Dominici 2014
41.55	1.57	F	Pellatispira madaraszi	36.0 ± 2.05	40 ± 40	528	0.016 ± 0.002	Pérez 2012
39.07	−9.20	F	Kentriodontidae indet.	8.47 ± 3.14	50 ± 50	98	$0.017 \pm^{0.019}_{0.009}$	(da Mata, 1962)

Table 1 *(continued)*

Lat	Long	Method	Fossil (e.g.)	Age (Ma)	PWD (m)	H (m)	Uplift rate	Study
42.77	−1.80	F	Bathysiphon spp.	39.7 ± 1.65	225 ± 75	468	0.017 ± 0.003	Astibia 2014
42.87	−2.08	F	Actinacis reussi	63.8 ± 2.20	25 ± 25	1,065	0.017 ± 0.001	Baceta 2005
41.38	1.62	F	Tarbellastraea reussiana	17.1 ± 3.31	25 ± 25	277	0.018 ± 0.005	(Chevalier, 1961)
41.93	2.30	F	Eurete n. sp. clava	40.0 ± 1.65	200 ± 50	502	0.018 ± 0.002	Taberner 1995
36.48	−5.00	F	Glycymeris bimaculata	3.96 ± 0.37	50 ± 50	29	$0.02 \pm^{0.016}_{0.013}$	Francisco 1993
37.27	−6.84	F	Carcharias taurus	4.47 ± 0.87	50 ± 50	39	$0.02 \pm^{0.019}_{0.013}$	García 2009
42.80	−1.55	F	Ammobaculites spp.	39.7 ± 1.65	150 ± 50	657	0.02 ± 0.002	Astibia 2014
38.25	−0.80	F	Sirenia indet.	8.47 ± 3.14	50 ± 50	126	$0.021 \pm^{0.022}_{0.010}$	(Sendra Saez & Hodgson, 1998)
42.89	−0.94	F	Eponides sp.	39.7 ± 1.65	50 ± 50	878	0.023 ± 0.002	Astibia 2005
42.38	0.52	F	Actinacis sp.	51.9 ± 4.10	150 ± 50	1,127	0.025 ± 0.003	Eichenseer 1992
40.76	0.59	F	Occitanomys sp.	4.47 ± 0.87	50 ± 50	64	$0.026 \pm^{0.020}_{0.014}$	(Agustí et al., 1983)
37.30	−1.88	F	Astadelphis gastaldii	4.47 ± 0.87	25 ± 25	99	$0.028 \pm^{0.014}_{0.009}$	(Sendra Saez & Hodgson, 1998)
42.41	1.82	F	Aturia (Aturia) ziczac	51.9 ± 4.10	350 ± 150	1,306	0.032 ± 0.005	Llompart 1986
37.28	−1.89	F	Cetacea indet.	3.09 ± 0.51	25 ± 25	87	$0.036 \pm^{0.016}_{0.012}$	Sendra 1999
37.33	−6.68	F	Isurus escheri	4.47 ± 0.87	50 ± 50	110	$0.036 \pm^{0.023}_{0.015}$	García 2009
37.33	−6.68	F	Isurus desori	4.47 ± 0.87	50 ± 50	113	$0.036 \pm^{0.023}_{0.015}$	García 2009
37.32	−6.67	F	Melanella (Balcis) lactea	4.47 ± 0.86	50 ± 50	109	$0.036 \pm^{0.023}_{0.015}$	(González Delgado, 1988)
42.50	−0.26	F	Stylocoenia n. sp.	40.0 ± 1.65	25 ± 25	1,413	0.036 ± 0.002	Altuna 2003
36.74	−2.63	M	-	0.130	-	4.94	$0.038 \pm^{0.008}_{0.015}$	Zazo 2003
36.97	−2.20	F	Bryozoa indet.	8.48 ± 3.14	2.5 ± 2.5	322	$0.038 \pm^{0.023}_{0.011}$	(Mankiewicz, 1996)
41.41	2.03	F	Pliophoca cf. etrusca	3.09 ± 0.51	50 ± 50	80	$0.042 \pm^{0.028}_{0.020}$	Mendez 2000
37.13	−2.10	F	Lithophyllum dentatum	8.47 ± 3.14	25 ± 25	439	$0.055 \pm^{0.037}_{0.017}$	Braga 2001
37.67	−1.73	F	Porites collegniana	8.48 ± 3.14	25 ± 25	530	$0.065 \pm^{0.043}_{0.020}$	Vennin 2004
37.07	−2.08	F	Lithothamnion sp.	7.60 ± 2.70	20 ± 20	515	$0.07 \pm^{0.016}_{0.012}$	Braga 2001
36.88	−2.30	F	Spondylus sp., Tapes sp.	3.09 ± 0.51	60 ± 40	174	$0.076 \pm^{0.030}_{0.022}$	Aguirre 1998
36.05	−5.63	M	-	0.099	-	11	$0.105 \pm^{0.046}_{0.084}$	Zazo 1999
37.02	−3.67	F	Lithothamnion sp.	9.43 ± 2.19	75 ± 25	940	$0.108 \pm^{0.036}_{0.022}$	Braga 2001
37.12	−3.53	F	Lithophyllum incrustans	9.43 ± 2.19	25 ± 25	1,005	$0.109 \pm^{0.036}_{0.022}$	Braga 2001
36.97	−3.70	F	Bryozoa indet.	8.48 ± 3.14	2.5 ± 2.5	1398	$0.165 \pm^{0.098}_{0.045}$	Braga 2001
37.43	−1.47	F	Strombus bubonius	0.069 ± 0.06	5 ± 5	9	$0.203 \pm^{1.908}_{0.133}$	Zazo 2003
36.70	−2.62	F	Patella sp.	0.069 ± 0.06	2.5 ± 2.5	13	$0.225 \pm^{1.775}_{0.123}$	Zazo 2003
36.72	−4.42	F	Glycymeris sp.	0.069 ± 0.06	10 ± 10	7	$0.247 \pm^{2.77536}_{0.192}$	Vera 2004

Note. Rates in top portion of the table were used to test predicted uplift rates, see body text (Figure 8). PWD = palaeo-water depth estimated by converting the palaeo-environment given in PaleoDB using Immenhauser (2009)'s scheme. H = Elevation of sample extracted from ASTER GDEM. Uplift rates are millimeter per year. Studies are lead author followed by year, see bibliography for full reference.

(Figure 5a). At face value, the distribution of marine fossils indicate that the central and coastal parts of the Pyrenees became terrestrial after ~60 and ~35 Ma, respectively. They show that southern Iberia experienced Neogene-Recent uplift, which corroborates our earlier synthesis of stratigraphic constraints.

An important consideration when calculating uplift from marine fauna is paleo-water depth, which we interpreted from the Paleobiological Database. Most Cenozoic Iberian marine fauna are suggestive of neritic environments, which yields a relatively small paleo-water depth correction (i.e., 0–150 m; Immenhauser, 2009). However, in some places fauna are indicative of bathyal environments, which result in larger errors. Stratigraphic ages and their uncertainties were extracted from the Paleobiological Database. We assumed that Cenozoic sea level varied by ±50 m, which is probably appropriate for the time scales of interest (e.g., Miller et al., 2005; Sidall et al., 2006). Our results are summarized in Figure 5. The age, elevation, and paleo-water depth of each sample was used to estimate cumulative and average rates of uplift

(Table 1). Average calculated uplift rates are O(10^{-3}–10^{-1}) mm/year and are highest on the southeastern coast (Figure 5b).

2.3. Marine Terraces: Radiometric Dating

Absolute dates exist for some marine terraces in southern and western Iberia. For example, U/Th dating of an 11-m high marine terrace from Tarifa, Gibraltar Strait, yields an age of 95 ± 10 ka and average uplift rates of $0.11^{+0.05}_{-0.08}$ mm/year (Zazo et al., 1999). A U-dated terrace from Casa de Renco, southeastern Iberia, yields an average uplift rate of $0.04^{+0.01}_{-0.02}$ mm/year (Zazo et al., 2003). Radiocarbon and optically stimulated luminescence dating of a suite of raised beaches indicate that parts of the Estremadura coastline, on Iberia's Atlantic margin, have been uplifted by tens of meters since ∼35–42 ka (Benedetti et al., 2009). Further south, close to Cadiz, 1–3 m high (above modern sea level), Upper Pleistocene beach and calcrete deposits have radiocarbon dating ages of ∼13–32 ka (Gracia et al., 2008). Figueiredo et al. (2014) correlated uplifted marine terraces along western and southwestern Portugal with Marine Isotope Stages to suggest average uplift rates of fractions of a millimeter per year since ∼330 ka.

2.4. Denudation and Rock Uplift: Thermochronometry

Histories of rock cooling, and by inference denudation and uplift, of some parts of Iberia have been constrained by thermochronometry (e.g., zircon, apatite fission tracks, U-Th/He; see, e.g., Juez-Larré & Ter Voorde, 2009). Calculated Cenozoic closure ages of a subset of samples are suggestive of Oligocene to Recent kilometer-scale erosional or tectonic denudation of large parts of the peninsula (e.g., Figure 5c). For example, high Miocene denudation rates (∼5–10 km/Ma) have been estimated radiometrically (e.g., whole-rock Rb-Sr, K-Ar and $^{40}Ar/^{39}Ar$) and from corroborative benthic foraminifera and nannoplanktonic observations in the southern part of the Betic Cordilleras (Zeck et al., 1992). Apatite fission track analyses of samples from the Betic Cordillera have closure ages of ∼16–2 Ma (Johnson, 1997). These results are broadly consistent with youngest fission track ages from samples in other parts of the cordillera and are generally interpreted as a record of tectonic and erosional denudation (Lonergan & Johnson, 1998; Platt et al., 2005). Across the Catalan Coastal Ranges zircon and apatite fission tracks ages have a broad spread of closure ages from 223–21 Ma, apatite (U-Th)/He ages vary between 58 ± 3 and 2 ± 0.2 Ma, which are interpreted as indicating $\lesssim$2 km of post-Oligocene exhumation, however the presence of high heat flow, hot springs, and mineralization, which are suggestive of advection of hot fluids, makes it difficult to assert a stable geotherm (Fernandez et al., 1998; Juez-Larré & Andriessen, 2006). Apatite (U-Th)/He data from the Sierra de Cameros, north-central Iberia, have closure ages of 43–30 Ma (Del Río et al., 2009). If we assume a geothermal gradient of 30 °C/km and (U-Th)/He closure temperatures of 60–70 °C, these results suggest that at least some parts of the Iberian Range have been exhumed by ∼1–2 km since ∼30 Ma, however, the geothermal gradient may have been higher (cf. Del Río et al., 2009). Apatite fission tracks analyses from the Pyrenees indicate closure ages of ∼35–13 Ma (Sinclair et al., 2005). Lower temperature apatite (U-Th)/He closure ages are broadly consistent with these results (Gibson et al., 2007). Collectively these thermochronometric constraints indicate that parts of southern and central Iberia, and the Pyrenean mountains, have experienced at least a kilometer of exhumation since ∼30 Ma. The timing of Neogene exhumation is broadly coeval with biostratigraphically constrained uplift (cf. Figure 5).

In summary, a broad suite of stratigraphic, biostratigraphic, radiogenic, and thermochronological data suggest Iberia has been uplifted and denuded during the last 30 Ma. Seismological observations combined with this inventory of uplift and denudation constraints indicate that evolution of the Pyrenees and Betics can be partially attributed to crustal thickening and loading. However, large parts of Iberia that have been uplifted at long wavelengths and denuded during the last 30 Ma are not associated with thick crust. These observations suggest that subcrust and perhaps subplate support might play an important role in governing the evolution of Iberian topography. The distribution of uplift and denudation measurements is clustered and is, in some places, sparse, which makes it challenging to reconstruct a Neogene history of dynamic support. We investigate whether these spot measurements can be augmented by inversion of drainage patterns.

3. Geomorphic Considerations

It is generally agreed that uplift and erosional processes control the shapes of drainage networks. The shapes of longitudinal river profiles (i.e., elevation as a function of distance), for example, appear to be sensitive to changing patterns of uplift and erosion (e.g., Anderson & Anderson, 2010). Consequently, a large body of work has focussed on extracting tectonic and erosional information from them (e.g., Howard, 1980;

Figure 6. Iberian drainage patterns. Black/colored curves = fluvial networks extracted from ASTER GDEM. Colored curves = major catchments: D = Duero; T = Tajo; Gi = Guadiana; Ga = Guadalquivir; S = Segura; E = Ebro.

Pritchard et al., 2009; Rosenbloom & Anderson, 1994; Stock & Montgomery, 1999; Whipple & Tucker, 1999). Inversion of large inventories of river profiles has shown that many fluvial networks contain commonalities that can be used to extract continental-scale histories of uplift and erosion (e.g., Paul et al., 2014; Roberts, White, et al., 2012; Wilson et al., 2014). The ubiquity of drainage patterns across Iberia indicates that inverting for a spatiotemporal history of uplift might be fruitful.

Drainage patterns were extracted across the peninsula from the ASTER digital elevation model, which has a horizontal resolution of ~30 m. The drainage network was extracted using ESRI's flow routing algorithms. First, local elevation pits and peaks were removed. Then flow directions, accumulation, and length were calculated from the "filled" digital elevation model using a D8 (steepest down-slope, near-neighbor) algorithm (Tarboton, 1997). The veracity of extracted drainage patterns was examined using satellite imagery (e.g., Landsat, Copernicus). The same flow routing process was performed using the SRTM 3-arc second (~90 m) digital elevation model to further examine fidelity of extracted drainage patterns. The final drainage network contains 3,217 rivers extracted from the ASTER digital elevation model (Figure 6a).

It is widely acknowledged that the shapes of river profiles depend on a combination of autogenic and allogenic processes operating at a range of wavelengths. For example, erosion rates at some scales are probably determined by the tensile and compressive strength of a river's substrate and by its orientation of joints and fractures (e.g., bedrock; Duvall et al., 2004). Biological activity and precipitation (discharge) also have important roles in determining the erosional efficacy of rivers at some scales (e.g., Roe et al., 2002; Whittaker & Boulton, 2012). It is, however, generally unclear how substrate translates into erodibility. Wavelet spectra of some river profiles provide some insights and suggests that most ($\gtrsim$90%) spectral power is generated at wavelengths greater than a few tens of kilometers, which suggests that short wavelength changes in substrate have a small effect on the shape of most river profiles (Roberts et al., 2019). Inverse modeling of river profiles suggests that changes in precipitation rate on time scales of less than a few million years (e.g., Milankovich cycles) do not significantly affect the shapes of longitudinal river profiles (e.g., Paul et al., 2014; Wilson et al., 2014). Notwithstanding these general statements, we compare the shapes of Iberia's principal rivers to substrate geology, biota, and precipitation (Figure 7).

Iberia's rivers cross a range of lithological contrasts. For example, the Tajo river, which drains central Iberia, flows through alternating Triassic and Jurassic rocks, a Neogene-Quaternary basin, Cambrian, Ordovician,

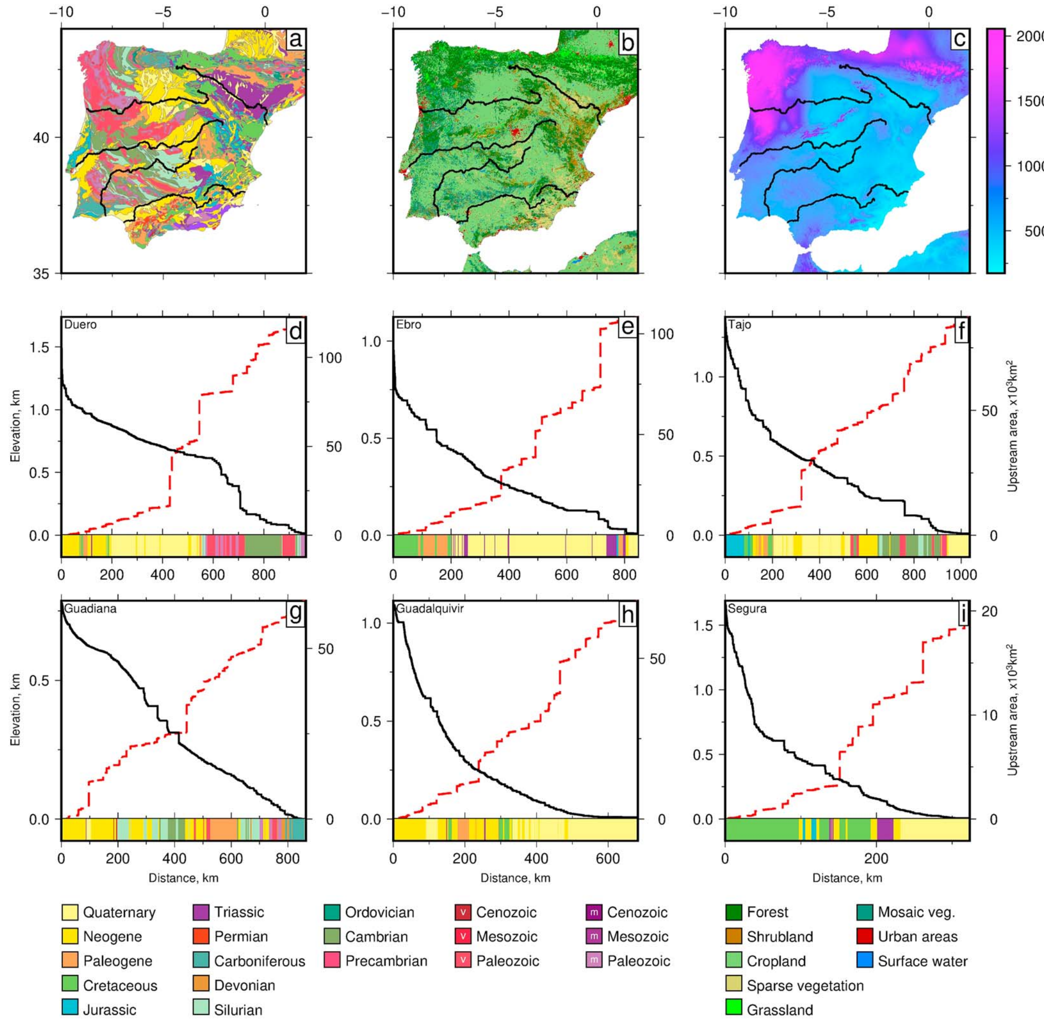

Figure 7. Lithology, biota, precipitation, and river profiles. Six major rivers atop (a) lithology from GEO42L model, v/m labels = igneous/metamorphic rocks (Pawlewicz et al., 1997); (b) Biota (Sayre et al., 2014), note legend bottom right of figure; (c) Precipitation (Fick & Hijmans, 2017). (d–i) Black lines = longitudinal river profiles for the major Iberian catchments shown in Figure 6; red dashed lines = calculated upstream drainage areas; colored barcode = lithology from GEO42L model.

and Palaeozoic igneous bedrock, Cenozoic deltaic deposits, and isolated Jurassic and Pre-Cambrian outcrops (Figure 7f). They also flow through a range of different biotic environments (Figure 7b). In general, Iberia's rivers flow from forest and shrubland, through cropland and grassland to mosaic vegetation on the western coast or sparse vegetation on the eastern coast. The modern Tajo, for example, originates in the forest and shrubland of the Montes Universales, flows through alternating cropland, mosaic vegetation, and forest of the Parque Natural do Tejo Internacional, and finally through Lisbon (Figure 7b). Modern precipitation rates are highest (>1,500 mm/year) in the northwest and throughout the Pyrenees mountains, they are lowest along the southern coast and in Iberia's interior (<500 mm/year, Figure 7c).

The longitudinal profiles of Iberia's six largest rivers—Duero, Ebro, Tajo, Guadiana, Guadalquivir, Segura—are shown in Figure 7. The Duero river, which drains northern Iberia, has a broad (~400 km long) knickzone (change in slope) centered at ~700 km distance from its head, which traverses a range of lithologies, biotic realms, and precipitation rates. This knickzone has ~600 m of relief. The Tajo river, draining central Iberia, has a large (~400 km long × 250 m relief) knickzone centered at ~800 km from its head. Similarly the Ebro, Guadiana, and Segura rivers contain broad, O(100) km wide, O(100) m relief knickzones. The correlation between the shapes of rivers in these six large catchments and changes in lithology, biota, or modern precipitation appears to be weak in general although the large knickzone on the Duero river coincides with Precambrian and metamorphic rock downstream of Neogene and Quaternary cover. Short, O(10) km, wavelength changes in substrate do not tend to correlate with changes in river shapes either (i.e., elevations, slopes, curvature), which is consistent with observations elsewhere (Paul et al., 2014; Roberts, White, et al., 2012).

These observations suggest that the shapes of most Iberian rivers contain long wavelength commonalities that are probably not controlled by substrate or modern precipitation patterns. Instead, these results suggest that inverting for histories of long wavelength uplift might compliment histories determined from stratigraphic observations. Our approach to constraining the evolution of Iberia's drainage patterns has four steps. First, we examine observations that constrain the history of uplift and erosion of Iberian rivers on time scales O(1–10) Ma. Second, we use these observations to calibrate a stream power erosional model. Third, this calibrated erosional model is used to invert our drainage inventory for a smooth, regularized, history of uplift. Finally, calculated uplift is compared to independent estimates of uplift extracted from the biostratigraphic and radiometric inventory of uplift spot measurements.

3.1. Drainage Patterns and Geomorphic Modeling

Mapping of fluvial terraces, morphometric analyses of longitudinal river profiles and planforms, landscape evolution models, and the stratigraphic archive have been used to constrain the evolution of fluvial processes throughout Iberia (e.g., Antón et al., 2012, 2014; Casas-Sainz & De Vicente, 2009; Cunha & Pereira, 2000; Cunha et al., 2005; Jones, 2002; Pérez-Peña et al., 2010; Santisteban & Schulte, 2007; Viveen et al., 2013). Rivers draining into the Atlantic Ocean and Mediterranean Sea contain fluvial terraces, which suggest that Iberia's rivers are responding to regional uplift (e.g., Cunha et al., 2005; Martins et al., 2009). The stratigraphic archive in Iberia's internal basins (e.g., Ebro, Duero) and estimates of sedimentary flux to its margins indicate that Iberian drainage, its sedimentary flux, and its routing systems have evolved throughout Neogene times (e.g., Evans & Arche, 2002; Fisher & Nichols, 2013). Rerouting of the Tajo and Duero rivers, for example, has been linked with Upper Miocene uplift of the Central System and Iberian Chain (Casas-Sainz & De Vicente, 2009). Parts of Iberia, notably the Duero and Ebro basins, were probably internally drained at various times during the Neogene (e.g., Antón et al., 2014; Fisher & Nichols, 2013; Garcia-Castellanos et al., 2003). The change from endorheic to exorheic drainage in these basins has been attributed to Neogene uplift (Casas-Sainz & De Vicente, 2009).

A body of work exists that makes use of the stream power erosional model (e.g., slope-area and “chi” analyses) to predict patterns of fluvial incision, longitudinal profiles, and drainage divide migration across Iberia (e.g., Giachetta et al., 2015; Vacherat et al., 2018). We investigate whether an inverse approach that makes use of a simple version of the stream power erosional model and smoothly varying uplift rates can be used to predict meaningful histories of uplift.

3.1.1. Erosional Model

Fluvial erosional models (e.g., stream power) are well documented (e.g., Howard, 1980; Rosenbloom & Anderson, 1994; Whipple & Tucker, 1999). In a simple form, they predict that the elevation of a river is controlled by rates of erosion, E, and uplift, U, both of which can vary as a function of space, x, and time, t,

$$\frac{\partial z}{\partial t} = -E(x,t) + U(x,t). \tag{2}$$

The crux of the problem in using such models to extract information about histories of uplift is parameterization of the erosional process. In principal, if histories of erosion are known one can solve for uplift histories using the shape of modern rivers. In some places, knickzones have been shown to propagate upstream with velocities that are broadly proportional to upstream drainage area (e.g., Czarnota et al., 2013; Stock & Montgomery, 1999). These observations are probably the strongest indication that fluvial erosion can be modeled using an advective scheme in which kinematic waves of erosion propagate headward. A relatively simple version of the stream power model that has been used to successfully invert for uplift histories can be expressed as

$$E = vA^m \left(\frac{\partial z}{\partial x}\right)^n, \tag{3}$$

where A is upstream drainage area and $\partial z/\partial x$ is slope. v determines the time scale of knickpoint retreat and must be calibrated independently (e.g., from geological measurements). v trades off with m, such that similar advective velocities can be achieved for different combinations of v and m (Roberts & White, 2010).

The distribution of best-fitting theoretical knickzones within families of drainage networks appears to be to some extent governed by the values of m and n. For example, Paul et al. (2014) found $n = 1$ yields the best fit to a large inventory of drainage patterns, which is concordant with some field evidence (e.g., Whittaker et al., 2007; Whittaker & Boulton, 2012). However, there is some debate about the values of n and if $n \neq 1$ shock waves can develop (see, e.g., Pritchard et al., 2009).

Slope-area analyses, and increasingly chi-elevation analyses, are favored methods for solving the stream power model and have been used on drainage networks through Iberia (e.g., Schoenbohm et al., 2004; Vacherat et al., 2018; Willett et al., 2014). However, both approaches have significant drawbacks if one wishes to solve for histories of uplift. Slope-area analyses assume that rivers, or their constituent tranches, are at steady state (e.g., $\partial z/\partial t = 0$), which in our view is almost never justified, and especially not for rivers that evolve on geological time scales. Furthermore, slope-area analyses necessarily requires differentiation of discrete and often noisy digital elevation data, which yields unstable solutions (see, e.g., Roberts, White, et al., 2012). Landscape response times can be calculated at continental-scales by integrating the stream power model (e.g., $\tau = \int \mathrm{d}x/vA^m$; Roberts, Paul, et al., 2012). However, we caution against the use of such metrics, including normalized versions (e.g., χ), to extract information about evolution of drainage networks (e.g., divide migration) because they fundamentally depend on where erosional signals are inserted, which is often poorly known. Another way to address this problem is to invert for spatiotemporal uplift histories using an integral approach to solve the stream power model. In that way one does not assume steady state, but allows for it, we do not have to differentiate the data, and the locations at which erosional signals are inserted into the model are not assumed a priori.

3.1.2. Inverse Modeling

Pritchard et al. (2009) and Roberts and White (2010) showed that individual river profiles can be inverted for uplift rate as a function of time. Roberts, White, et al. (2012) and Paul et al. (2014) solved the more general problem to invert multiple river profiles for uplift rate as a function of space and time. They investigated the effects of changing erosional parameters (e.g., $m,\ n$) and precipitation rates for calculated uplift histories and shapes of theoretical river profiles. Goren et al. (2014) created a linear Bayesian approach to invert drainage patterns for uplift rate histories. Rudge et al. (2015) showed that smooth histories of uplift can be extracted from continental-drainage networks using a linearized approach without recourse to prior information. These linear models are considerably quicker than the more general numerical optimization models. There is a growing literature focussed on the development and application of such inverse approaches to understand fluvial landscape evolution (see, e.g., Campforts & Govers, 2015; Croissant & Braun, 2014; Fox et al., 2014; Glotzbach, 2015).

We followed the methodology described in Rudge et al. (2015) to invert Iberia's drainage network for spatiotemporal histories of uplift rate. First, the method of characteristics is used to solve the stream power model for each river, producing two general solutions in integral form

$$\tau_g = \int_0^{x(t)} \frac{\mathrm{d}x}{vA^m}, \tag{4}$$

$$z^* = \int_0^{\tau_g} U(x(t), t)\mathrm{d}t, \tag{5}$$

assuming boundary conditions

$$x = x^*, z = z^* \text{ at } t = 0 \tag{6}$$

and

$$x = 0, z = 0 \text{ at } t = \tau_g. \tag{7}$$

Today at position x^*, elevation is z^*. At a given time, τ_g, the river profile intersects the river mouth ($x = 0$) at sea level ($z = 0$). Uplift rates are defined at discrete spatial and temporal nodes, producing $\mathbf{U}$, a vector of values (see, e.g., Figure A1 in ; Rudge et al., 2015). Our model is discretized using a regular spatial grid that is composed of triangles and is evenly sampled in time. Vertex spacing was 40 km and 0.9 Ma. The starting set of $\mathbf{U}$ in the inverse model is the null set. Given positions x^*, integration of equation (4) gives characteristic

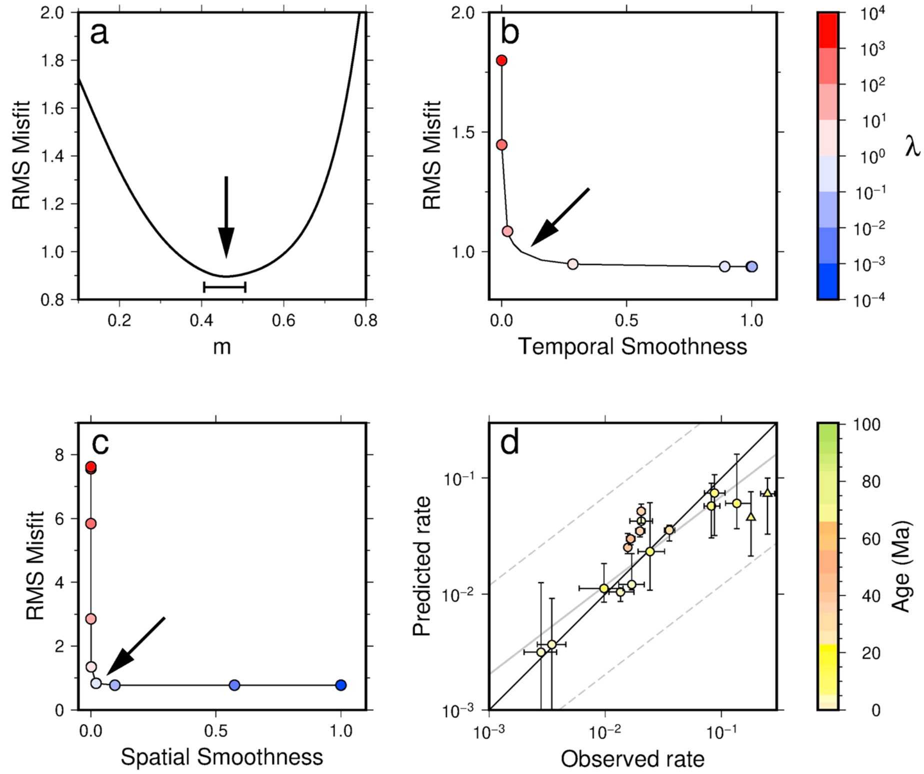

Figure 8. Calibration of erosional model. (a) Residual rms misfit as a function of erosional parameter, m. Arrow = value of preferred model. Bar = models with low residual misfit. (b) Data misfit as a function of model smoothness for range of temporal smoothing values, λ_t. Arrow = optimal value. In these tests λ_s was 0. (c) Data misfit as a function of spatial smoothing. (d) Observed versus predicted uplift rates. Circles = uplift rates and errors calculated from palaeontological data (see Table 1). Triangles = uplift rates and errors from dated marine terraces (e.g., Zazo et al., 1999, 2003; Table 1). Errors in predicted rates = range of values in a 30-km annulus. Diagonal black line = 1:1 match. Solid gray line = linear regression of observed versus predicted rates; $r^2 = 0.66$. Dashed gray lines = regression of observed versus calculated uplift rates for two scenarios in which v was increased or decreased by an order of magnitude. rms = root-mean-square.

curves. The trapezoidal rule is used in combination with these characteristic curves to discretize equation (5) and produce a matrix equation for a set of elevations, $\mathbf{z}$,

$$\mathbf{z} = M\mathbf{U}. \tag{8}$$

This matrix equation is then inverted using a nonnegative linear least squares approach to find uplift values, $\mathbf{U}$. Since M is often undetermined damping is required, and we minimize

$$|M\mathbf{U} - \mathbf{z}|^2 + \lambda_S^2|S\mathbf{U}|^2 + \lambda_T^2|T\mathbf{U}|^2, \quad \text{subject} \quad \text{to} \quad \mathbf{U} \geq 0, \tag{9}$$

where λ_S and λ_T are the spatial and temporal smoothing parameters, respectively. The spatial smoothing matrix, S, is given by

$$|S\mathbf{U}|^2 = \int_s \int_{t=0}^{t_{max}} |\nabla U|^2 \quad \mathrm{d}t\,\mathrm{d}S, \tag{10}$$

and the temporal smoothing matrix, T, by

$$|T\mathbf{U}|^2 = \int_s \int_{t=0}^{t_{max}} \left|\frac{\partial U}{\partial t}\right|^2 \quad \mathrm{d}t\,\mathrm{d}S. \tag{11}$$

Following calibration of erosional parameters we can invert for regional uplift histories.

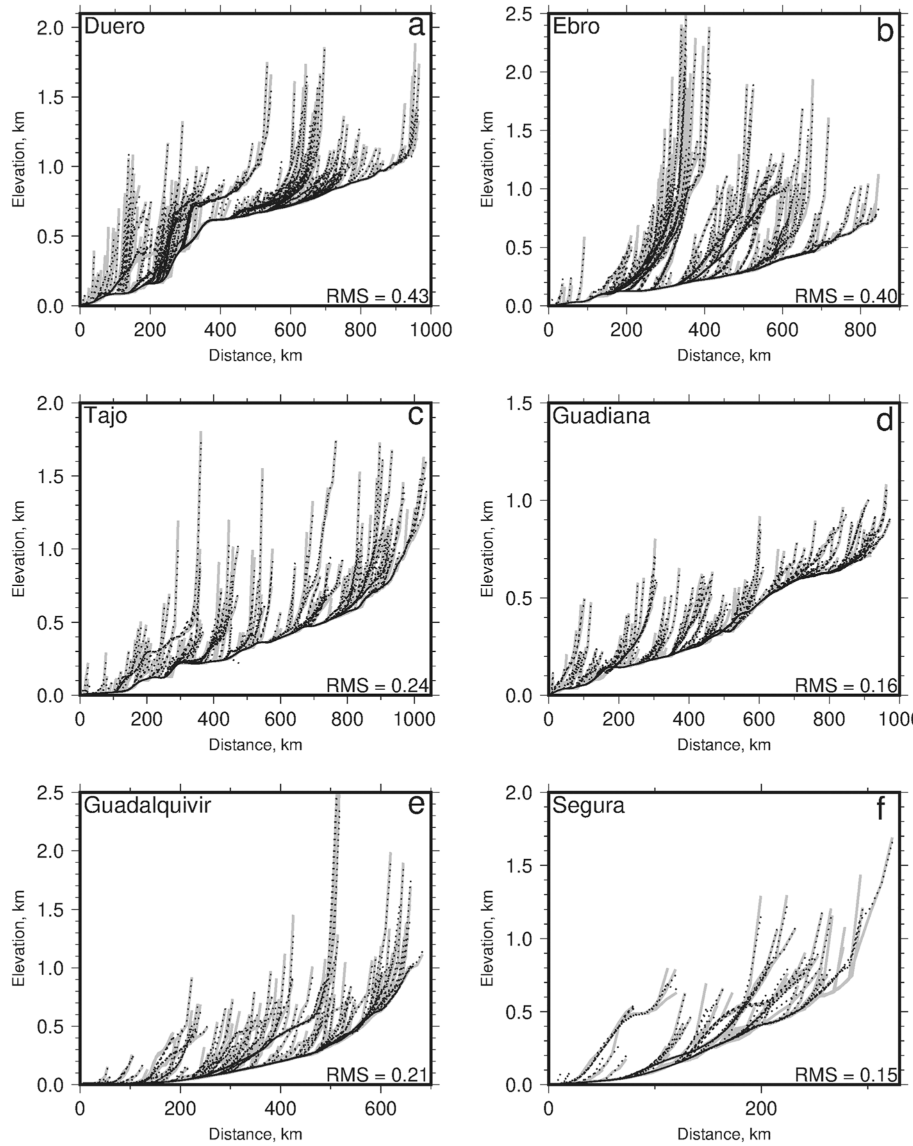

Figure 9. Longitudinal river profiles. (a-f) Observed (gray) and best-fitting theoretical (dotted) longitudinal river profiles for the major Iberian catchments shown in Figure 6. Theoretical river profiles were produced by uplift history shown in Figure 10. Residual rms misfit is shown for each catchment; global residual rms misfit = 0.96. rms = root-mean-square.

3.1.3. Model Calibration and Damping

An important feature of inverse modeling is that the effect erosional and damping parameters have on results can be objectively assessed by calculating residual root-mean-square (rms) misfit between observed and calculated river profiles. We calculate rms misfit as

$$\sqrt{\frac{1}{K}\sum_{ij=1}^{I,J}\left(\frac{z^o_{ij}-z^c_{ij}}{\sigma_{ij}}\right)^2}, \tag{12}$$

where j is number of river profiles, i is number of points on a given profile, K is the total number of points, z^o and z^c are observed and calculated river profile elevations, σ is the uncertainty in elevation, which we set to 20 m. Following Paul et al. (2014) and Giachetta et al. (2015) we set $n = 1$ and performed a suite of tests in which the erosional parameter m was systematically varied between 0.1 and 0.8. The lowest residual rms misfit between observed and theoretical rivers was obtained for $m = 0.44$ (Figure 8a). The value of v was set so that calculated uplift of the Pyrenees postdates the age of the youngest marine sample in our

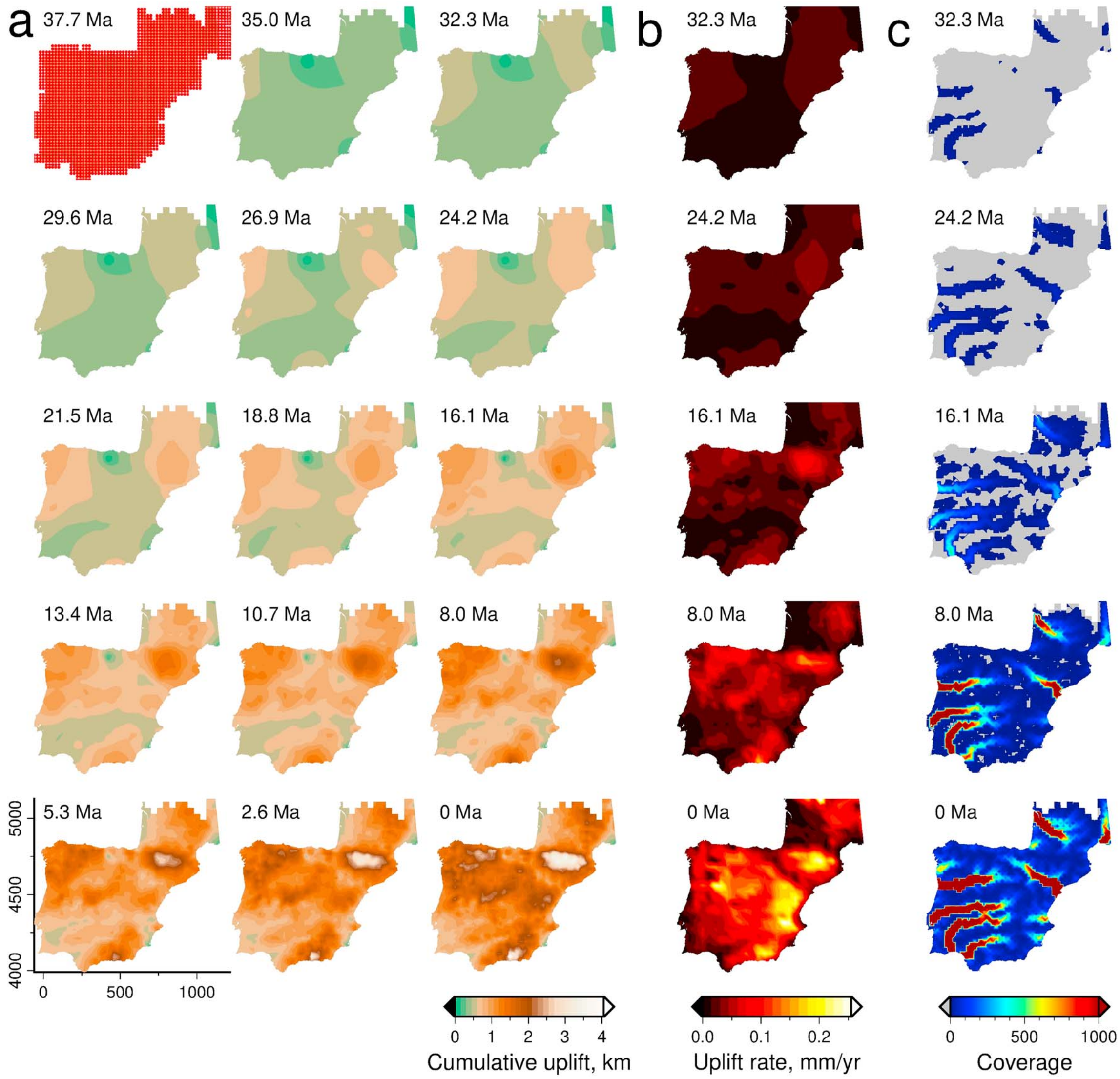

Figure 10. Calculated uplift history. (a) Calculated cumulative uplift history from 37.7 Ma to present. Red dots = vertices at which uplift is inserted into the model. (b) Calculated uplift rates. (c) Number of nonzero entries in the model matrix at each node, that is, model coverage. High coverage equates to higher model confidence.

Pyrenean biostratigraphic data set (35 Ma; Figure 5a). We used a value of $v = 1.11$ m^{1-2m}/Ma to invert Iberia's drainage patterns. To test the sensitivity of our results to the value of v we increased or decreased its value by an order of magnitude and reinverted the drainage inventory (Figure 8d).

Smoothing parameters, λ_s and λ_t, control the spatial and temporal smoothing of calculated uplift, respectively. Following Parker (1994)'s protocol we sought the smoothest model that yielded the minimum misfit. Figure 8 shows residual rms misfit plotted as a function of model misfit for a range of λ values. The optimal values of $\lambda_S = 0.25$ and $\lambda_T = 4$. Global residual rms misfit is 0.96. Residual rms misfit of the major drainage basins is between 0.15 and 0.43 (Figure 9). Model coverage is highest for cells that intersect the downstream trunks of major rivers and decreases significantly at ages older than ~30 Ma as expected (see Figure 10c).

3.1.4. Calculated Uplift History

The calculated history of uplift spans 60 Ma (Figure 10a). The earliest calculated uplift occurred along the northwest coast at 35 Ma, Pyrenean growth followed at 32 Ma, originating from a central rise and spread coastward. Pyrenean uplift rates increase with time and peak during the last 5 Ma. Uplift of the Cantabrian mountains occurred between ~27 and 2 Ma, beginning on the western coast. From 18 Ma to present, uplift migrated southeast initiating growth of the Central Spanish System. The Iberian Chain grew at rates of up

10.1029/2018GC007899

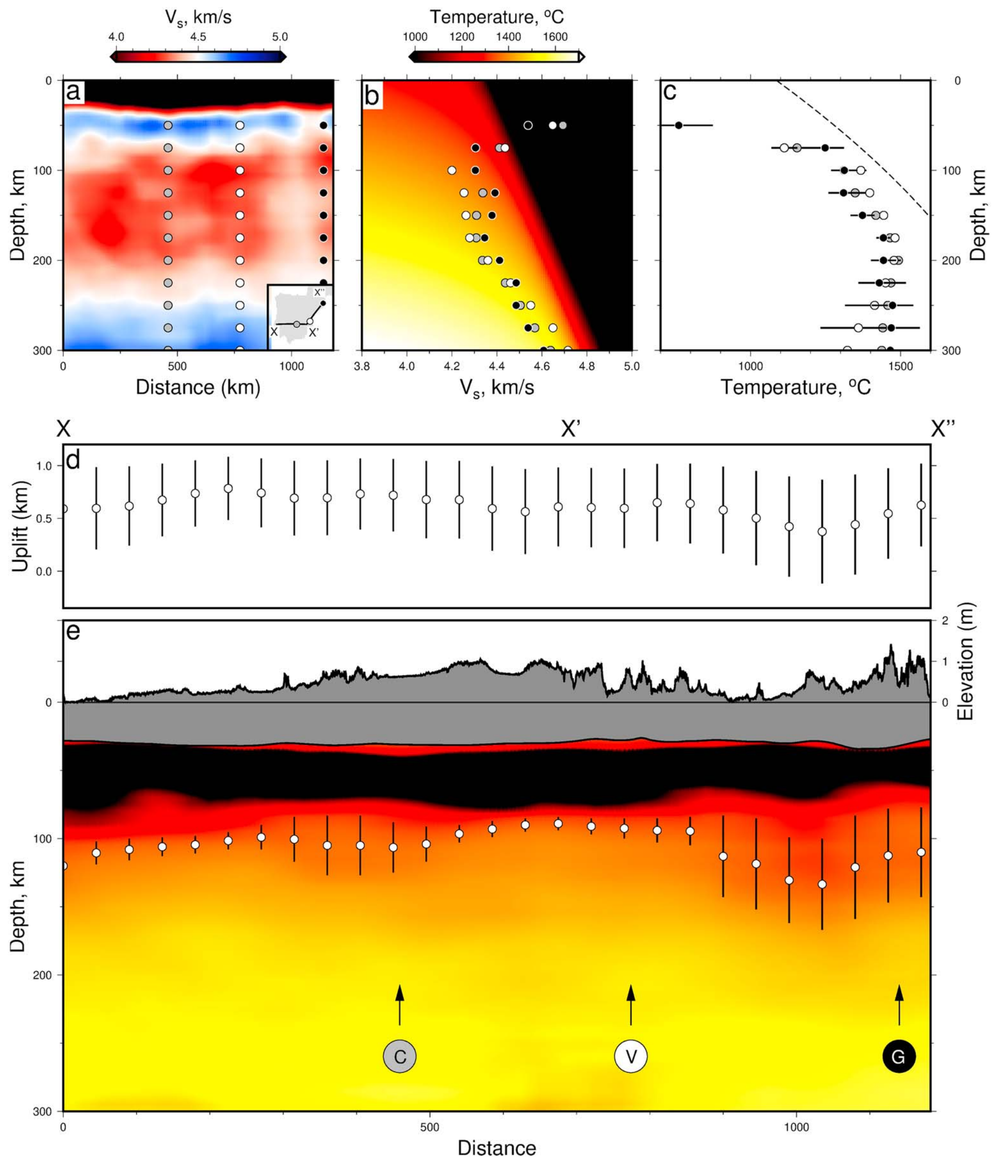

Figure 11. Shear wave to temperature conversion. (a) Dog-leg cross section through shear wave model designed to intersect volcanic regions (updated from Fichtner & Villaseñor, 2015; see inset map). Gray/white/black circles = velocities extracted at locations shown on inset map (Calatrava/Valencia/Catalan). (b) Look-up chart showing temperature as a function of depth (pressure) and velocity from Priestley and McKenzie (2006)'s parameterization. Gray/white/black circles = velocity-depth values for locations shown in panel (a). (c) Geotherms calculated at locations shown in panel (a); error bars = range of value for Priestley and McKenzie (2006) and Goes et al. (2000) parameterizations of $V_S(P, T)$; dashed line = dry peridotite solidus (Katz et al., 2003). (d) Uplift calculated along X – X′–X″ transect; error bars = range of values for Priestley and McKenzie (2006) and Goes et al. (2000) parameterizations (see body text for details). (e) Topography, crustal, and lithospheric thicknesses atop temperature/depth model calculated using Priestley and McKenzie (2006) parameterization along transect; circles with error bars = 1330 °C isotherm (base of the plate) from Priestley and McKenzie (2006) and Goes et al. (2000) parameterizations. Black curve = crustal thicknesses extracted from gridded receiver function synthesis (see Figure 1; Mancilla & Diaz, 2015). Note change in vertical scale. Labeled circles = locations shown in panel (a) centered on Calatrava (C), Valencia (V), and Catalan (Garrotxa; G) volcanic fields; note coincident relatively shallow and warm asthenosphere.

to ~0.24 mm/year. Calculated uplift of the Betic Cordillera initiated at ~17 Ma and has had rates of up to ~0.23 mm/year.

4. Discussion

4.1. Fidelity of Calculated Uplift

Calculated cumulative uplift unsurprisingly resembles a smooth version of modern topography (Figure 10a). The inventory of independent uplift constraints estimated using dated marine terraces and biostratigraphic observations can be used to test our results (Figures 5 and 8 and Table 1). We used the fossils with small palaeo-water depth errors ($\lesssim$20 m) that came from marine terraces with ages greater than the temporal resolution of our model (~1 Myr) to test our predictions. These observations result in the smallest uncertainties in measured uplift rates. A linear regression between calculated and observed uplift rates is shown as the gray line in Figure 8. It lies close to the 1:1 line and has an r^2 values of 0.66. The dashed lines in Figure 8 show linear regressions for models where v has been either increased or decreased by an order of magnitude, which clearly yield poor matches to independent uplift estimates and suggest that our chosen value for v is of the correct order.

Another constraint on the history of Iberian landscape and lithospheric evolution is exhumation recorded by low temperature thermochronometry (Figure 5c). Converting rock cooling estimates into denudation, uplift, or changes in structural relief is not trivial. Denudation is probably not equivalent to uplift in many circumstances. However, denudation can drive rock uplift via isostatic adjustment and rock uplift can drive denudation by generating changes in potential energy on broadly comparable time scales (e.g., base-level changes). Therefore, it can be informative to compare histories of denudation and rock uplift. We note that the timing of calculated uplift is broadly consistent with exhumation recorded by apatite fission track and U-Th/He thermochronometry across Iberia. For example, Fitzgerald et al. (1999), Metcalf et al. (2009), and Beamud et al. (2011) estimated rapid Oligocene exhumation in the Pyrenees beginning on the south flank of the axial zone using apatite fission track thermochronology. Our calculated history of uplift predicts initial Pyrenean uplift at ~32 Ma, which is broadly coeval with this phase of exhumation. Gibson et al. (2007) estimated exhumation rates in the Pyrenees of up to 1.5 mm/year at ~30 Ma, slowing to 0.1 mm/year at ~20 Ma. Metcalf et al. (2009) discovered a second phase of rapid exhumation beginning at 5 Ma, our model predicts an increase in uplift rate at ~5 Ma.

De Vicente et al. (2007) studied apatite fission tracks in the Central Spanish System and noted a significant increase in exhumation at ~10 Ma, which is broadly coeval with a phase of rapid uplift predicted by our model. Thermochronometric constraints from the Betics indicate rapid exhumation between ~19 and 16 Ma and a second phase since 5 Ma (Sosson et al., 1998). Our model predicts rapid uplift of the Betics at ~17 Ma.

These results suggest that as well as undergoing Cenozoic shortening and subsidence Iberia also experienced kilometer-scale Neogene epeirogenic uplift and denudation. Basaltic magmatism and slow shear wave velocity anomalies indicates that subplate support might have played an important role in generating Neogene uplift, which we examine in the following section.

4.2. Subplate Thermal Anomalies

To investigate the role of asthenospheric temperatures in generating support we first convert our updated full waveform shear wave model to temperature and then calculate upper mantle isostatic support. A cross section of seismic velocities through Iberia, which intersects the Calatrava, Valencia, and Catalan volcanic provinces is shown in Figure 11. Seismic velocities as a function of pressure (depth, z) beneath Iberia have been converted into temperature using Priestley and McKenzie (2006)'s $V_s(P, \Theta, a)$ empirical parameterization, where P is pressure, Θ is temperature in °C, and a encapsulates the activation process. Their conversion scheme can be expressed as

$$V_s = \{1 + b_v(z - 50)\} \left\{ m\Theta + c + A \exp\left(\frac{-E - PV_a}{RT}\right)\right\}, \tag{13}$$

where empirical constants $b_v = 3.84 \times 10^{-4}$ km^{-1}, $m = -2.8 \times 10^{-1}$ m·s^{-1} · $\oint$C^{-1}, c = 4,720 m/s, $A = -1.8 \times 10^{16}$ m/s, and activation energy and volume are $E = 409 \times 10^3$ J/mol and $V_a = 10 \times 10^{-6}$ m^3/mol, respectively, R is the gas constant and T is temperature in Kelvin. Pressure was assumed to be lithostatic such that $P = \rho g z$, where ρ = 3,300 kg/m^3, which yields $P \approx 30z$ MPa, if z has units of meters.

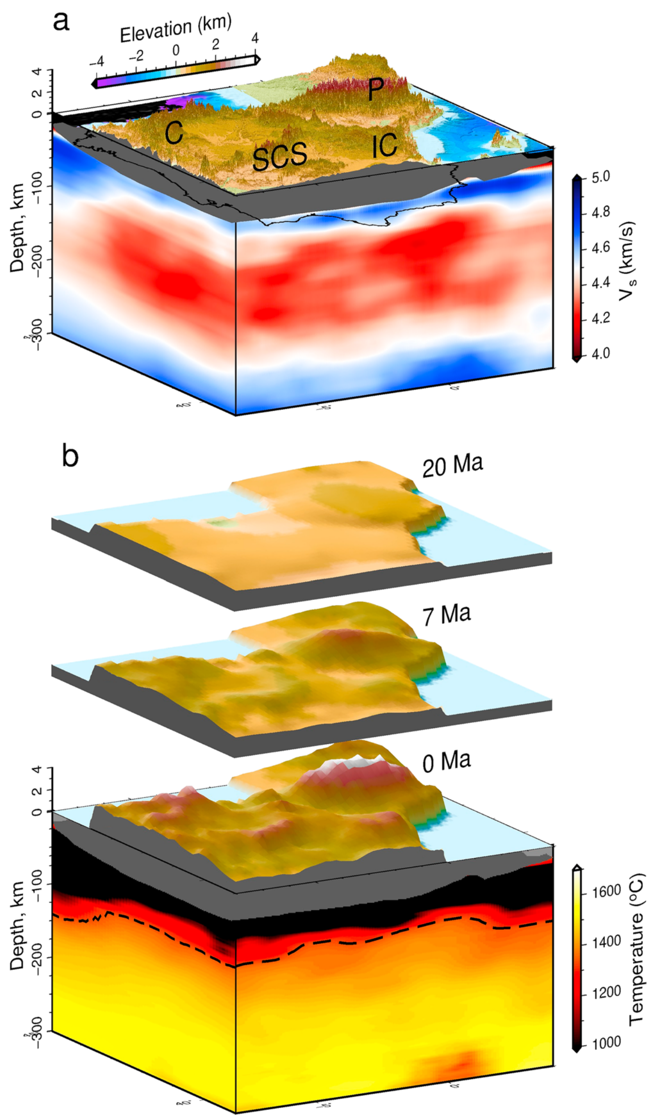

Figure 12. A history of Iberian epeirogeny. (a) Iberian topography and crustal thickness (gray polygons) atop slices through shear wave tomographic model; P = Pyrenees; C = Cantabrian Mountains; IC = Iberian Chain; SCS = Spanish Central System. Thin black line = projected coastline. (b) Calculated cumulative uplift at 20, 7, and 0 Ma. Box shows calculated cumulative uplift at 0 Ma atop cross sections through upper mantle thermal structure calculated using Priestley and McKenzie (2006)'s parameterization. Dashed lines = calculated 1330 °C isotherm.

Equation (13) was used to generate the look up chart shown in Figure 11 from which temperatures can be readily extracted as function of depth and V_s.

Calculated temperatures were compared to Goes et al. (2000)'s mineral physics-based parameterization (Figure 11c; see Lodhia et al., 2018). Figure 11c shows temperatures beneath the Calatrava and Catalan volcanic provinces and the Valencia volcanic zone. The highest calculated temperatures (1492 ± 14 °C) are beneath the Calatrava volcanic province, which has young (1.8–7.6 Ma) basaltic magmatism (Figure 11c; Cebriá & Lopez-Ruiz, 1995). Here the 1330 °C isotherm here is calculated to be shallow (~100 km) and ≲100 km beneath much of central Iberia. Uncertainties in temperatures were calculated from the range predicted by Priestley and McKenzie (2006) and Goes et al. (2000)'s parameterizations.

To estimate topographic support, U, generated by asthenosphere thermal anomalies we use a simple isostatic calculation

$$U = \frac{h\alpha\overline{T}}{1-\alpha T_{\circ}}, \tag{14}$$

10.1029/2018GC007899

where h is thickness of the asthenospheric channel, thermal expansivity $\alpha = 3.28 \times 10^{-5}$ °K^{-1}, $\overline{T}$ is average excess temperature between 100 and 300 km, and $T_\circ$ is background temperature, which we set to 1330 °C (Rudge et al., 2008). An estimate of asthenospheric support with a channel thickness of 200 km is shown in Figure 11d. Uncertainties show the range of values calculated using the Priestley and McKenzie (2006) and Goes et al. (2000) parameterizations. Average excess asthenospheric temperatures beneath Calatrava and Catalan volcanic provinces are estimated to be 96 and 82 °C, which indicates isostatic support of 0.4–1.0 and 0.3–0.9 km, respectively. The measured elevations at these two locations are 0.8 and 1.0 km, respectively. Average calculated asthenospheric isostatic support of Iberia is $\gtrsim$0.4 km almost everywhere.

We suggest that asthenospheric temperature anomalies beneath most of Iberia are sufficiently high to account for 0.4–0.8 km of its long wavelength ($\gtrsim$100 km) topography. Histories of uplift indicate that these thermal anomalies grew during the last ∼30 Ma (Figure 12). We note that Iberian plate motions have been small during this time, which might have facilitated the expression of subplate thermal anomalies in Iberian topography (e.g., Seton et al., 2012). Crustal thickness changes and loading of the lithosphere in the Pyrenees, Iberian Chain, and Betic Cordilleria have played important roles in generating vertical motions at shorter wavelengths (see, e.g., Banks & Warburton, 1991; Muñoz, 1992; Vissers et al., 1995).

5. Conclusions

Seismological observations (e.g., receiver functions), simple isostatic calculations, and the transfer function between gravity and topography indicate that not all of Iberia's topography is supported by changes in crustal thickness or flexural responses to loading of the plate. Instead, full waveform shear wave tomography and extrusive magmatism suggest that the mantle beneath Iberia is anomalously warm. Young intraplate magmatic provinces (e.g., Calatrava, Catalan) appear to sit atop asthenosphere with positive excess temperatures. Conversion of the shear wave model into temperature and simple isostatic calculations indicate that ∼0.4–0.8 km of Iberia topography is supported by the uppermost convecting mantle. We investigated the timing of growth of this topographic support using an inventory of biostratigraphic and absolute dating of uplifted terraces and marine rock. These observations were augmented by inversion of 3,217 longitudinal river profiles. Calculated uplift rates match independent uplift rates obtained from the fossil and uplifted marine rock database. Calculated uplift rates are O(10^{-3}–10^{-1}) mm/year during the last 30 Ma. We suggest that calculated uplift combined with seismological and magmatic observations indicate that Neogene epeirogeny of Iberia was a response to the development of thermal anomalies with excess temperatures of O(10–100)°K beneath the Iberian plate.

Acknowledgments
We thank P. Ball, V. Fernandes, A. Lipp, S. Goes, L. Lonergan, D. Rood, A. Seal, N. White, and A. Whittaker for helpful discussion. SRTM data can be downloaded from http://srtm.csi.cgiar.org. ASTER data can be downloaded from https://asterweb.jpl.nasa.gov. PaleoDB data can be downloaded from https://paleobiodb.org.

References

Aguirre, J., Braga, J. C., & Bassi, D. (2011). Taxonomic assessment of coralline algal species (Rhodophyta; Corallinales and Sporolithales) described by Pfender, Lemoine, and Miranda from northern Spain type localities. *Annalen des Naturhistorischen Museums in Wien. Serie A für Mineralogie und Petrographie, Geologie und Paläontologie, Anthropologie und Prähistorie*, *113*, 267–289.

Aguirre, J., & Jiménez, A. (1998). Fossil analogues of present-day Cladocora Caespitosa coral banks: Sedimentary setting, dwelling community, and taphonomy (late Pliocene, W Mediterranean)'. *Coral Reefs*, *17*(3), 203–213.

Agustí, J., Anadón, P., Arbiol, S., Cabrera, L., Colombo, F., & Sáez, A. (1987). Biostratigraphical characteristics of the Oligocene sequences of North-Eastern Spain (Ebro and Campins basins). *Münchner Geowissenschaftliche Abhandlungen, A*, *10*, 35–42.

Agustí, J., Anadó, P., & Juliá Brugués, R. (1983). Nuevos datos sobre el Plioceno del Baix Ebre. Aportación a la correlación entre las escalas marina y continental. *Acta Geológica Hispánica*, *18*(2), 123–130.

Alonso, A., Floquet, M., Mas, R., & Meléndez, A. (1993). Late Cretaceous carbonate platforms: Origin and evolution, Iberian range, Spain. *AAPG Mem*, *56*, 297–313.

Altuna, A., Alvarez-Pérez, G., Busquets, P., & Etayo, V. (2003). Five new species of Bartonian (Eocene) corals: Jaca basin, Pyrenees, Spain. *Fossil corals and sponges. Proceedings of 9th international symposium on fossil Cnidaria and Porifera, Osterr Akad Wiss Schriftenreihe Erdwiss Wien'*, *1*, 435–453.

Alvarez-Valero, A. M., & Kriegsman, L. M. (2007). Crustal thinning and mafic underplating beneath the Neogene Volcanic Province (Betic Cordillera, SE Spain): Evidence from crustal xenoliths. *Terra Nova*, *19*, 266–271.

Anderson, R. S., & Anderson, S. P. (2010). *Geomorphology: The mechanics and chemistry of landscapes*. Cambridge: Cambridge University Press.

Andeweg, B. (2002). *Cenozoic tectonic evolution of the Iberian Peninsula: Effects and causes of changing stress fields*. Amsterdam: Vrije Universiteit Amsterdam.

Andriessen, P., & Zeck, H. P. (1996). Fission-track constraints on timing of alpine nappe emplacement and rates of cooling and exhumation, Torrox area, Betic Cordilleras, S. Spain. *Chemical Geology*, *131*(1-4), 199–206.

Antón, L., De Vicente, G., Muñoz-Martín, A., & Stokes, M. (2014). Using river long profiles and geomorphic indices to evaluate the geomorphological signature of continental scale drainage capture, Duero basin (NW Iberia). *Geomorphology*, *206*, 250–261.

Antón, L., Rodés, A., De Vicente, G., Pallàs, R., Garcia-Castellanos, D., Stuart, F. M., et al. (2012). Quantification of fluvial incision in the Duero basin (NW Iberia) from longitudinal profile analysis and terrestrial cosmogenic nuclide concentrations. *Geomorphology*, *165*, 50–61.

Astibia, H., Elorza, J., Pisera, A., Alvarez-Pérez, G., Payros, A., & Ortiz, S. (2014). Sponges and corals from the middle Eocene (Bartonian) marly formations of the Pamplona Basin (Navarre, Western Pyrenees): Taphonomy, taxonomy, and paleoenvironments'. *Facies*, *60*(1), 91–110.

Astibia, H., Payros, A., Suberbiola, X. P., Elorza, J., Berreteaga, A., Etxebarria, N., et al. (2005). Sedimentology and taphonomy of sirenian remains from the Middle Eocene of the Pamplona basin (Navarre, Western Pyrenees). *Facies*, *50*(3-4), 463–475.

Baceta, J. I., Pujalte, V., & Bernaola, G. (2005). Paleocene coralgal reefs of the western Pyrenean basin, Northern Spain: New evidence supporting an earliest Paleogene recovery of reefal ecosystems. *Palaeogeography, Palaeoclimatology, Palaeoecology*, *224*(1), 117–143.

Banks, C. J., & Warburton, J. (1991). Mid-crustal detachment in the Betic system of southeast Spain. *Tectonophysics*, *191*(3-4), 275–289.

Barton, P., & Wood, R. (1984). Tectonic evolution of the North Sea basin: Crustal stretching and subsidence. *Geophysical Journal of the Royal Astronomical Society*, *79*(3), 987–1022.

Beamud, E., Muñoz, J. A., Fitzgerald, P. G., Baldwin, S. L., Garcés, M., Cabrera, L., & Metcalf, J. R. (2011). Magnetostratigraphy and detrital apatite fission track thermochronology in syntectonic conglomerates: Constraints on the exhumation of the South-Central Pyrenees. *Basin Research*, *23*(3), 309–331.

Becker, J., Sandwell, D., Smith, W., Braud, J., Binder, B., Depner, J., et al. (2009). Global bathymetry and elevation data at 30 arc seconds resolution: SRTM30_plus. *Marine Geodesy*, *32*(4), 355–371.

Belaústegui, Z., de Gibert, J. M., Domènech, R., Muñiz, F., & Martinell, J. (2011). Tafonomía y contexto paleoambiental de los restos de un Cetáceo del Mioceno medio de Tarragona (NE España). *Geobios*, *44*(1), 19–31.

Benedetti, M. M., Haws, J. A., Funk, C. L., Daniels, J. M., Hesp, P. A., Bicho, N. F., et al. (2009). Late Pleistocene raised beaches of coastal Estremadura, Central Portugal. *Quaternary Science Reviews*, *28*(27-28), 3428–3447.

Betzler, C., Braga, J. C., Martín, J. M., Sanchez-Almazo, I. M., & Lindhorst, S. (2006). Closure of a seaway: Stratigraphic record and facies (Guadix basin, Southern Spain). *International Journal of Earth Sciences*, *95*(5), 903–910.

Bozdag, E., & Trampert, J. (2008). On crustal corrections in surface wave tomography. *Geophysical Journal International*, *172*, 1066–1082.

Braga, J. C., & Aguirre, J. (1995). Taxonomy of fossil coralline algal species: Neogene lithophylloideae (rhodophyta, corallinaceae) from southern Spain'. *Review of Palaeobotany and Palynology*, *86*(3-4), 265–285.

Braga, J. C., & Aguirre, J. (2001). Coralline algal assemblages in upper Neogene reef and temperate carbonates in southern Spain. *Palaeogeography, Palaeoclimatology, Palaeoecology*, *175*(1), 27–41.

Braga, J. C., Martin, J. M., & Alcala, B. (1990). Coral reefs in coarse-terrigenous sedimentary environments (Upper Tortonian, Granada Basin, southern Spain). *Sedimentary Geology*, *66*(1-2), 135–150.

Braga, J. C., Martín, J. M., & Quesada, C. (2003). Patterns and average rates of late Neogene–Recent uplift of the Betic Cordillera, SE Spain. *Geomorphology*, *50*(1-3), 3–26.

Braga, J. C., Vescogni, A., Bosellini, F. R., & Aguirre, J. (2009). Coralline algae (Corallinales, Rhodophyta) in western and central Mediterranean Messinian reefs. *Palaeogeography, Palaeoclimatology, Palaeoecology*, *275*(1), 113–128.

Campforts, B., & Govers, G. (2015). Keeping the edge: A numerical method that avoids knickpoint smearing when solving the stream power law. *Journal of Geophysical Research: Earth Surface*, *120*, 1189–1205. https://doi.org/10.1002/2015JF003602

Carballo, A., Fernández, M., Jiménez-Munt, I., Torné, M., Vergés, J., Melchiorre, M., et al. (2015). From the North-Iberian margin to the Alboran basin: A lithosphere geo-transect across the Iberian plate. *Tectonophysics*, *663*, 399–418.

Casas-Sainz, A., & De Vicente, G. (2009). On the tectonic origin of Iberian topography. *Tectonophysics*, *474*(1-2), 214–235.

Cebriá, J.-M., & Lopez-Ruiz, J. (1995). Alkali basalts and leucitites in an extensional intracontinental plate setting: The late Cenozoic Calatrava volcanic province (central Spain)'. *Lithos*, *35*(1-2), 27–46.

Cebriá, J., López-Ruiz, J., Doblas, M. d. l., Oyarzun, R., Hertogen, J., & Benito, R. (2000). Geochemistry of the quaternary alkali basalts of Garrotxa (NE volcanic province, Spain): A case of double enrichment of the mantle lithosphere. *Journal of Volcanology and Geothermal Research*, *102*(3), 217–235.

Chevalier, J. P. (1961). Recherches sur les Madréporaires et les formations récifales Miocènes de la Méditerranée occidentale. *These, Paris, 959., Mém. Soc. Géol. Fr., N.S*, *40*(93), 562.

Cloetingh, S., Burov, E., Beekman, F., Andeweg, B., Andriessen, P., Garcia-Castellanos, D., et al. (2002). Lithospheric folding in Iberia. *Tectonics*, *21*(5), 1041. https://doi.org/10.1029/2001TC901031

Colli, L., Ghelichkhan, S., & Bunge, H.-P. (2016). On the ratio of dynamic topography and gravity anomalies in a dynamic Earth. *Geophysical Research Letters*, *43*, 2510–2516. https://doi.org/10.1002/2016GL067929

Croissant, T., & Braun, J. (2014). Constraining the stream power law: A novel approach combining a landscape evolution model and an inversion method. *Earth Surface Dynamics*, *2*, 155–166.

Cunha, P. P., Martins, A. A., Daveau, S., & Friend, P. (2005). Tectonic control of the Tejo river fluvial incision during the late Cenozoic, in Ródao–Central Portugal (Atlantic Iberian border). *Geomorphology*, *64*(3-4), 271–298.

Cunha, P. P., & Pereira, D. I. (2000). Evolução Cenozóica da área de Longroiva-Vilariça (NE Portugal). *Ciencias de Terra (UNL), Lisboa*, *14*, 89–98.

Czarnota, K., Hoggard, M., White, N., & Winterbourne, J. (2013). Spatial and temporal patterns of Cenozoic dynamic topography around Australia. *Geochemistry, Geophysics, Geosystems*, *14*, 634–658.

d'Estevou, P. O., & Termier, G. (1978). Etude preliminaire des spongiaires Tortoniens du bassin de Sorbas (Espagne Meridionale); indications bathymetriques. *Bulletin de la Société géologique de France*, *7*(3), 315–318.

da Mata, C. R. (1962). Nota preliminar sobre um delfinídeo (Eurhinodelphis cf. cristatus) do Miocénio do Penedo, a Norte do Cabo Espichel. *Boletim do Museu e Laboratório Mineralógico e Geológico da Faculdade de Ciências, Universidade de Lisboa*, *9*, 157–166.

da Silva, C. M., Landau, B., Domènech, R., & Martinell, J. (2010). Pliocene Atlantic molluscan assemblages from the Mondego Basin (Portugal): Age and palaeoceanographic implications. *Palaeogeography, Palaeoclimatology, Palaeoecology*, *285*(3), 248–254.

de Bruijne, C. H., & Andriessen, P. A. M. (2002). Far field effects of Alpine plate tectonism in the Iberian microplate recorded by fault-related denudation in the Spanish Central System. *Tectonophysics*, *349*(1-4), 161–184.

De Vicente, G., Cloetingh, S., Van Wees, J. D., & Cunha, P. P. (2011). Tectonic classification of Cenozoic Iberian foreland basins. *Tectonophysics*, *502*, 38–61.

De Vicente, G., Vegas, R., Martín, A. M., Silva, P., Andriessen, P., Cloetingh, S., et al. (2007). Cenozoic thick-skinned deformation and topography evolution of the Spanish Central System. *Global and Planetary Change*, *58*(1), 335–381.

Del Río, P., Barbero, L., & Stuart, F. (2009). Exhumation of the Sierra de Cameros (Iberian Range, Spain): Constraints from low-temperature thermochronology. *Geological Society, London, Special Publications*, *324*(1), 153–166.

Díaz, J., & Gallart, J. (2009). Crustal structure beneath the Iberian Peninsula and surrounding waters: A new compilation of deep seismic sounding results. *Physics of the Earth and Planetary Interiors*, *173*(1-2), 181–190.

Díaz, J., Villaseñor, A., Gallart, J., Morales, J., Pazos, A., Cordoba, D., et al. TopoIberia Seismic Working Group (2009). The IBERARRAY broadband seismic network: A new tool to investigate the deep structure beneath Iberia. *ORFEUS Newsletter*, *8*, 1–6.

Dominici, S., & Kowalke, T. (2014). Early Eocene cerithioidean gastropods of mangrove-fringed coasts (south–central Pyrenees, Spain). *Bollettino della Società Paleontologica Italiana*, *53*(3), 137–162.

Duggen, S., Hoernle, K., van den Bogaard, P., & Garbe-Schönberg, D. (2005). Post-collisional transition from subduction-to intraplate-type magmatism in the Westernmost Mediterranean: Evidence for continental-edge delamination of subcontinental lithosphere. *Journal of Petrology*, *46*(6), 1155–1201.

Duggen, S., Hoernle, K., van den Bogaard, P., & Harris, C. (2004). Magmatic evolution of the Alboran region: The role of subduction in forming the Western Mediterranean and causing the Messinian salinity crisis. *Earth and Planetary Science Letters*, *218*(1), 91–108.

Duvall, A., Kirby, E., & Burbank, D. (2004). Tectonic and lithologic controls on bedrock channel profiles and processes in coastal California. *Journal of Geophysical Research*, *109*, F03002. https://doi.org/10.1029/2003JF000086

Eichenseer, H., & Luterbacher, H. (1992). The marine Paleogene of the Tremp region (NE Spain)-depositional sequences, facies history, biostratigraphy and controlling factors. *Facies*, *27*(1), 119–151.

Esteban, M. (1996). An overview of Miocene reefs from Mediterranean areas: General trends and facies models. In *Models for carbonate stratigraphy* (pp. 3–55). Oklahoma. https://doi.org/10.2110/csp.96.05

Esteban, J. J., Sánchez-Rodríguez, L., Seward, D., Cuevas, J., & Tubía, J. M. (2004). The late thermal history of the Ronda area, Southern Spain. *Tectonophysics*, *389*(1-2), 81–92.

Estevens, M. (2000). Miocene marine mammals from Portugal, paleogeographical and paleoecological significance. *Cirências da Terra (UNL), Lisboa*, *14*, 323–334.

Evans, G., & Arche, A. (2002). The flux of siliciclastic sediment from the Iberian Peninsula, with particular reference to the Ebro. *Geological Society, London, Special Publications*, *191*(1), 199–208.

Fernandez, M., Marzan, I., Correia, A., & Ramalho, E. (1998). Heat flow, heat production, and lithospheric thermal regime in the Iberian Peninsula. *Tectonophysics*, *291*, 29–53.

Fichtner, A., & van Leeuwen, T. (2015). Resolution analysis by random probing. *Journal of Geophysical Research: Solid Earth*, *120*, 5549–5573. https://doi.org/10.1002/2015JB012106

Fichtner, A., & Villaseñor, A. (2015). Crust and upper mantle of the western Mediterranean–Constraints from full-waveform inversion. *Earth and Planetary Science Letters*, *428*, 52–62.

Fick, S. E., & Hijmans, R. J. (2017). Worldclim 2: New 1-km spatial resolution climate surfaces for global land areas. *International Journal of Climatology*, *37*(12), 4302–4315.

Figueiredo, P. M., Cabral, J., & Rockwell, T. K. (2014). Recognition of Pleistocene marine terraces in the southwest of Portugal (Iberian Peninsula): Evidences of regional Quaternary uplift. *Annals of Geophysics*, *56*(6), 1–19. https://doi.org/10.4401/ag-6276

Fisher, J. A., & Nichols, G. J. (2013). Interpreting the stratigraphic architecture of fluvial systems in internally drained basins. *Journal of the Geological Society*, *170*(1), 57–65.

Fitzgerald, P., Muñoz, J., Coney, P., & Baldwin, S. (1999). Asymmetric exhumation across the Pyrenean orogen: Implications for the tectonic evolution of a collisional orogen. *Earth and Planetary Science Letters*, *173*(3), 157–170.

Forst, M. H., Brachert, T. C., & Pais, J. (2000). High-resolution correlation of coastal cliff sections in the Lagos-Portimao formation (lower-middle Miocene, central Algarve, Portugal). *Giências da,Terra*, *14*, 289–296.

Förste, C., Bruinsma, S., Flechtner, F., Marty, J., Lemoine, J., Dahle, C., et al. (2012). A preliminary update of the direct approach GOCE processing and a new release of EIGEN-6c. In *'AGU Fall meeting abstracts'*. Washington, DC: American Geophysical Union.

Fox, M., Goren, L., May, D. A., & Willett, S. D. (2014). Inversion of fluvial channels for paleorock uplift rate in Taiwan. *Journal of Geophysical Research: Earth Surface*, *119*, 1853–1875. https://doi.org/10.1002/2014JF003196

Francisco, M. L., Peláez, J. V., & Guerra-Merchán, A. (1993). Arcoida (Mollusca, Bivalvia) del Plioceno de la provincia de Málaga, España. *Treballs del Museu de Geologia de Barcelona*, *3*, 157–187.

García, M., Xio, E., Telles-Antunes, M., Cáceres-Balbino, A., Ruiz-Muñoz, F., & Civis-Llovera, J. (2009). Los tiburones Lamniformes (Chondrichthyes, Galeomorphii) del Plioceno inferior de la Formación Arenas de Huelva, suroeste de la cuenca del Guadalquivir, España. *Revista Mexicana de Ciencias Geológicas*, *26*(3), 674–686.

Garcia-Castellanos, D., Vergés, J., Gaspar-Escribano, J., & Cloetingh, S. (2003). Interplay between tectonics, climate, and fluvial transport during the Cenozoic evolution of the Ebro basin (NE Iberia). *Journal of Geophysical Research*, *108*(B7), 2347. https://doi.org/10.1029/2002JB002073

Gaspar-Escribano, J., Van Wees, J., Ter Voorde, M., Cloetingh, S., Roca, E., Cabrera, L., et al. (2001). Three-dimensional flexural modelling of the Ebro basin (NE Iberia). *Geophysical Journal International*, *145*(2), 349–367.

Geel, T., Roep, T. B., Ten Kate, W., & Smit, J. (1992). Early-middle Miocene stratigraphic turning points in the Alicante region (SE Spain): Reflections of Western Mediterranean plate-tectonic reorganizations. *Sedimentary Geology*, *75*(3-4), 223–239.

Giachetta, E., Molin, P., Scotti, V. N., & Faccenna, C. (2015). Plio-Quaternary uplift of the Iberian chain (Central–Eastern Spain) from landscape evolution experiments and river profile modeling. *Geomorphology*, *246*, 48–67.

Gibson, M., Sinclair, H. D., Lynn, G. J., & Stuart, F. M. (2007). Late- to post-orogenic exhumation of the Central Pyrenees revealed through combined thermochronological data and modelling. *Basin Research*, *19*(3), 323–334.

Glotzbach, C. (2015). Deriving rock uplift histories from data-driven inversion of river profiles. *Geology*, *43*, 467–470.

Goes, S., Govers, R., & Vacher, P. (2000). Shallow mantle temperatures under Europe from P and S wave tomography. *Journal of Geophysical Research*, *105*(B5), 11,153–11,169.

González Delgado, J. Á. (1988). Estudio sistemático de los gasterópodos del Plioceno de Huelva (SW de España). III. Mesogastropoda (Scalacea-Tonnacea). *Stvdia Geologica Salmanticensia*, *XXV*, 109–160.

Goren, L., Fox, M., & Willett, S. D. (2014). Tectonics from fluvial topography using formal linear inversion: Theory and applications to the Inyo Mountains, California. *Journal of Geophysical Research: Earth Surface*, *119*, 1651–1681. https://doi.org/10.1002/2014JF003079

Gracia, F., Rodríguez-Vidal, J., Cáceres, L., Belluomini, G., Benavente, J., & Alonso, C. (2008). Diapiric uplift of an MIS 3 marine deposit in SW Spain: Implications for late Pleistocene sea level reconstruction and palaeogeography of the Strait of Gibraltar. *Quaternary Science Reviews*, *27*(23-24), 2219–2231.

Howard, A. D. (1980). Thresholds in river regimes. *Thresholds in Geomorphology*, *227*, 227–258.

Immenhauser, A. (2009). Estimating palaeo-water depth from the physical rock record. *Earth-Science Reviews*, *96*(1), 107–139.

Janssen, M., Thorne, M., Cloetingh, S., & Banda, E. (1993). Pliocene uplift of the Eastern Iberian margin: Inferences from quantitative modelling of the Valencia Trough. *Earth and Planetary Science Letters*, *119*(4), 585–597.

Johnson, C. (1997). Resolving denudational histories in orogenic belts with apatite fission-track thermochronology and structural data: An example from Southern Spain. *Geology*, *25*(7), 623–626.

Jones, S. J. (2002). Transverse rivers draining the Spanish Pyrenees: Large scale patterns of sediment erosion and deposition. *Geological Society, London, Special Publications*, *191*(1), 171–185.

Juez-Larré, J., & Andriessen, P. (2006). Tectonothermal evolution of the Northeastern margin of Iberia since the break-up of Pangea to present, revealed by low-temperature fission-track and (U–Th)/He thermochronology: A case history of the Catalan coastal ranges. *Earth and Planetary Science Letters*, *243*(1-2), 159–180.

Juez-Larré, J., & Ter Voorde, M. (2009). Thermal impact of the break-up of Pangea on the Iberian Peninsula, assessed by thermochronological dating and numerical modelling. *Tectonophysics*, *474*(1-2), 200–213.

Katz, R. F., Spiegelman, M., & Langmuir, C. H. (2003). A new parameterization of hydrous mantle melting. *Geochemistry, Geophysics, Geosystems*, *4*(9), 1073. https://doi.org/10.1029/2002GC000433

Llompart Díaz, C. (1986). Restos de nautílidos en la secuencia deposicional de armàncies (Eoceno, Prepirineo de Girona). *Scientia gerundensis*, *12*, 165.

Lodhia, B. H., Roberts, G. G., Fraser, A. J., Fishwick, S., Goes, S., & Jarvis, J. (2018). Continental margin subsidence from shallow mantle convection: Example from West Africa. *Earth and Planetary Science Letters*, *481*, 350–361.

Lonergan, L., & Johnson, C. (1998). Reconstructing orogenic exhumation histories using synorogenic detrital zircons and apatites: An example from the Betic Cordillera, SE Spain. *Basin Research*, *10*(3), 353–364.

Mancilla, F., & Diaz, J. (2015). High resolution Moho topography map beneath Iberia and Northern Morocco from receiver function analysis. *Tectonophysics*, *663*, 203–211.

Mankiewicz, C. (1996). The middle to upper Miocene carbonate complex of Nijar, Almeria province, southeastern Spain. In *Models for carbonate stratigrahy from Miocene reef complexes of Mediterranean regions, SEPM Concepts in Sedimentology and Paleontology 5* (pp. 141–157). Oklahoma: Society for Sedimentary Geology.

Martí, J., Mitjavila, J., Roca, E., & Aparicio, A. (1992). Cenozoic magmatism of the Valencia trough (western Mediterranean): Relationship between structural evolution and magmatism. *Tectonophysics*, *203*, 145–165.

Martins, A., Cunha, P. P., Huot, S., Murray, A., & Buylaert, J.-P. (2009). Geomorphological correlation of the tectonically displaced Tejo river terraces (Gavião–Chamusca area, Central Portugal) supported by luminescence dating. *Quaternary International*, *199*(1-2), 75–91.

McKenzie, D. (2003). Estimating Te in the presence of internal loads. *Journal of Geophysical Research*, *108*(B9), 2438. https://doi.org/10.1029/2002JB001766

McKenzie, D. (2010). The influence of dynamically supported topography on estimates of Te. *Earth and Planetary Science Letters*, *295*(1-2), 127–138.

McKenzie, D., & Fairhead, D. (1997). Estimates of the effective elastic thickness of the continental lithosphere from Bouguer and free air gravity anomalies. *Journal of Geophysical Research*, *102*(B12), 27,523–27,552.

Mendez, J., Galobart, A., & Llenas, M. (2000). Sobre la presencia de Pliophoca etrusca (Tavani, 1941) en el Plioceno Catalan. *Batalleria*, *9*, 23–28.

Metcalf, J. R., Fitzgerald, P. G., Baldwin, S. L., & Muñoz, J.-A. (2009). Thermochronology of a convergent orogen: Constraints on the timing of thrust faulting and subsequent exhumation of the Maladeta pluton in the central Pyrenean axial zone. *Earth and Planetary Science Letters*, *287*(3), 488–503.

Miller, K. G., Kominz, M. A., Browning, J. V., Wright, J. D., Mountain, G. S., Katz, M. E., et al. (2005). The Phanerozoic record of global sea-level change. *Science*, *310*(5752), 1293–1298.

Morris, R., Sinclair, H., & Yelland, A. (1998). Exhumation of the Pyrenean orogen: Implications for sediment discharge. *Basin Research*, *10*(1), 69–85.

Morsilli, M., Bosellini, F. R., Pomar, L., Hallock, P., Aurell, M., & Papazzoni, C. A. (2012). Mesophotic coral buildups in a prodelta setting (late Eocene, southern Pyrenees, Spain): A mixed carbonate–siliciclastic system. *Sedimentology*, *59*(3), 766–794.

Muñoz, J. A. (1992). Evolution of a continental collision belt: ECORS-Pyrenees crustal balanced cross-section. In *Thrust tectonics*. (pp. 235–246). London: Chapman and Hall.

Muñoz-Martín, A., De Vicente, G., Fernández-Lozano, J., Cloetingh, S., Willingshofer, E., Sokoutis, D., & Beekman, F. (2010). Spectral analysis of the gravity and elevation along the Western Africa–Eurasia plate tectonic limit: Continental versus oceanic lithospheric folding signals. *Tectonophysics*, *495*(3-4), 298–314.

Murillas, J., Mougenot, D., Boulot, G., Comas, M., Banda, E., & Mauffret, A. (1990). Structure and evolution of the Galicia interior basin (Atlantic western Iberian continental margin). *Tectonophysics*, *184*(3-4), 297–319.

Pais, J. (2004). The Neogene of the lower Tagus basin (Portugal). *Revista Española de Paleontología*, *19*(2), 229–242.

Pais, J., Cunha, P. P., Pereira, D., Legoinha, P., Dias, R., Moura, D., et al. (2012). *The Paleogene and Neogene of western Iberia (Portugal): A Cenozoic record in the European Atlantic domain, in 'The Paleogene and Neogene of Western Iberia (Portugal)'* (pp. 1–138). Berlin: Springer.

Palomeras, I., Villanseñor, A., Thurner, S., Levander, A., Gallart, J., & Harnafi, M. (2017). Lithospheric structure of Iberia and Morocco using finite-frequency Rayleigh wave tomography from earthquakes and seismic ambient noise. *Geochemistry, Geophysics, Geosystems*, *18*, 1824–1840. https://doi.org/10.1002/2016GC006657

Parker, R. L. (1994). *Geophysical inverse theory*. Princeton: Princeton University Press.

Paul, J. D., Roberts, G. G., & White, N. (2014). The African landscape through space and time. *Tectonics*, *33*, 898–935. https://doi.org/10.1002/2013TC003479

Pawlewicz, M. J., Steinshouer, D. W., & Gautier, D. L. (1997). Map showing geology, oil and gas fields, and geologic provinces of Europe including Turkey (*Open File Report 97–4701*). USGS Technical report.

Pérez, G. A., & Buezo, P. B. (2012). Formas anómalas en los corales Eocenos de la Cuenca de Igualada (Noreste de España). *Revista Española de Paleontología*, *27*(1), 15–28.

Pérez-Peña, J. V., Azor, A., Azañón, J. M., & Keller, E. A. (2010). Active tectonics in the Sierra Nevada (Betic Cordillera, SE Spain): Insights from geomorphic indexes and drainage pattern analysis. *Geomorphology*, *119*(1-2), 74–87.

Pisera, A., Cachao, M., & Da Silva, C. M. (2006). Siliceous sponge spicules from the Miocene Mem Moniz marls (Portugal) and their environmental significance. *Rivista Italiana di Paleontologia e Stratigrafia (Research In Paleontology and Stratigraphy)*, *112*(2), 287–299.

Platt, J., Argles, T., Carter, A., Kelley, S., Whitehouse, M., & Lonergan, L. (2003). Exhumation of the Ronda peridotite and its crustal envelope: Constraints from thermal modelling of a P–T–time array. *Journal of the Geological Society*, *160*(5), 655–676.

Platt, J., Kelley, S., Carter, A., & Orozco, M. (2005). Timing of tectonic events in the Alpujárride complex, Betic Cordillera, southern Spain. *Journal of the Geological Society*, *162*(3), 451–462.

Pomar, L., Baceta, J. I., Hallock, P., Mateu-Vicens, G., & Basso, D. (2017). Reef building and carbonate production modes in the West-Central Tethys during the Cenozoic. *Marine and Petroleum Geology*, *83*, 261–304.

Priestley, K., & McKenzie, D. (2006). The thermal structure of the lithosphere from shear wave velocities. *Earth and Planetary Science Letters*, *244*(1), 285–301.

Pritchard, D., Roberts, G., White, N., & Richardson, C. (2009). Uplift histories from river profiles. *Geophysical Research Letters*, *36*, L24301. https://doi.org/10.1029/2009GL040928

Quintana, L., Pulgar, J., & Alonso, J. (2015). Displacement transfer from borders to interior of a plate: A crustal transect of iberia. *Tectonophysics*, *663*, 378–398.

Redaccion, A., & Saragossa, A. (2001). El fosil de una ballena confirma la riqueza paleontologica marina de Rojales y Guadiamar. *Aragonia*, *7*, 20–21.

Roberts, G. G., Paul, J. D., White, N., & Winterbourne, J. (2012). Temporal and spatial evolution of dynamic support from river profiles: A framework for Madagascar. *Geochemistry, Geophysics, Geosystems*, *13*, Q04004. https://doi.org/10.1029/2012GC004040

Roberts, G. G., & White, N. (2010). Estimating uplift rate histories from river profiles using African examples. *Journal of Geophysical Research*, *115*, B02406. https://doi.org/10.1029/2009JB006692

Roberts, G. G., White, N., & Lodhia, B. H. (2019). The generation and scaling of longitudinal river profiles. *Journal of Geophysical Research: Earth Surface*, *124*. https://doi.org/10.1029/2018JF004796

Roberts, G., White, N., Martin-Brandis, G., & Crosby, A. (2012). An uplift history of the Colorado Plateau and its surroundings from inverse modeling of longitudinal river profiles. *Tectonics*, *31*, TC4022. https://doi.org/10.1029/2012TC003107

Roe, G. H., Montgomery, D. R., & Hallet, B. (2002). Effects of orographic precipitation variations on the concavity of steady-state river profiles. *Geology*, *30*(2), 143–146.

Rosenbloom, N. A., & Anderson, R. S. (1994). Hillslope and channel evolution in a marine terraced landscape, Santa Cruz, California. *Journal of Geophysical Research*, *99*(B7), 14,013–14,029.

Rudge, J. F., Champion, M. E. S., White, N., McKenzie, D., & Lovell, B. (2008). A plume model of transient diachronous uplift at the Earth's surface. *Earth and Planetary Science Letters*, *267*(1-2), 146–160.

Rudge, J. F., Roberts, G. G., White, N. J., & Richardson, C. N. (2015). Uplift histories of Africa and Australia from linear inverse modeling of drainage inventories. *Journal of Geophysical Research: Earth Surface*, *120*, 894–914. https://doi.org/10.1002/2014JF003297

Ruiz, J., Gomez-Ortiz, D., & Tejero, R. (2006). Effective elastic thicknesses of the lithosphere in the Central Iberian Peninsula from heat flow: Implications for the rheology of the continental lithospheric mantle. *Journal of Geodynamics*, *41*(5), 500–509.

Sanchez-Marco, A. (2003). A paleospecies of alca (Aves: Charadriiformes) in the Pliocene of Spain. *Neus Jahrbuch fur Palaeontologie*, *5*, 314–320.

Santisteban, J. I., & Schulte, L. (2007). Fluvial networks of the Iberian Peninsula: A chronological framework. *Quaternary Science Reviews*, *26*(22-24), 2738–2757.

Sayre, R., Dangermond, J., Frye, C., Vaughan, R., Aniello, P., Breyer, S., et al. (2014). A new map of global ecological land units—An ecophysiographic stratification approach. https://doi.org/10.13140/2.1.2167.8887

Schoenbohm, L., Whipple, K., Burchfiel, B., & Chen, L. (2004). Geomorphic constraints on surface uplift, exhumation, and plateau growth in the Red river region, Yunnan Province, China. *Geological Society of America Bulletin*, *116*(7-8), 895–909.

Sendra, J., Bajo, I., & Cardenas, J. (1996). Un ejemplar de Misticeto (Mammalia: Cetacea) del Plioceno inferior de Alcalá de Guadaira (Sevilla). *Jornadas de Paleontologia*, *12*, 116–117.

Sendra, J., & De Renzi, M. (1995). Mamíferos marinos fósiles del Neógeno del sur de Alicante. *Comunicaciones de las XI Jornadas de Paleontologia*, 165–166.

Sendra, J., & De Renzi, M. (1999). A taphonomical study of marine mammals from the Almería region, SE Spain, *'BSRG/BGRG SE Spain field meeting guide book* (pp. 169–176). England': University of Plymouth.

Sendra Saez, J., & Hodgson, D. (1998). Astadelphis gastaldii (Brandt, 1874) - Mammalia, Cetacea, Delphinidae - en el Plioceno Espanol. *Jornada de Paleontologia*, *14*, 169–172.

Serra Kiel, J., Mató, E., Saula, E., Travé i Herrero, A., Ferrández i Cañadell, C., Tosquella i Angrill, J., et al. (2003). An inventory of the marine and transitional middle/upper Eocene deposits of the southeastern Pyrenean foreland basin (NE Spain). *Geologica Acta*, *1*, 2. https://doi.org/10.1344/105.000001610

Seton, M., Müller, R. D., Zahirovic, S., Gaina, C., Torsvik, T., Shephard, G., et al. (2012). Global continental and ocean basin reconstructions since 200 Ma. *Earth-Science Reviews*, *113*(3), 212–270.

Sidall, M., Chappell, J., & Potter, E. (2006). Eustatic sea-level during past interglacials. In *The climate of past interglacials* (pp. 75–92). Amsterdam: Elsevier.

Sinclair, H., Gibson, M., Naylor, M., & Morris, R. (2005). Asymmetric growth of the Pyrenees revealed through measurement and modeling of orogenic fluxes. *American Journal of Science*, *305*(5), 369–406.

Sorbi, S., Domning, D. P., Vaiani, S. C., & Bianucci, G. (2012). Metaxytherium subapenninum (Bruno, 1839)(Mammalia, Dugongidae), the latest sirenian of the Mediterranean Basin. *Journal of Vertebrate Paleontology*, *32*(3), 686–707.

Sosson, M., Morrillon, A.-C., Bourgois, J., Féraud, G., Poupeau, G., & Saint-Marc, P. (1998). Late exhumation stages of the Alpujarride Complex (western Betic Cordilleras, Spain): New thermochronological and structural data on Los Reales and Ojen nappes. *Tectonophysics*, *285*(3), 253–273.

Stock, J. D., & Montgomery, D. R. (1999). Geologic constraints on bedrock river incision using the stream power law. *Journal of Geophysical Research*, *104*(B3), 4983–4993.

Taberner, C., & Bosence, D. (1985). *Ecological succession from corals to coralline algae in Eocene patch reefs, Northern Spain, in 'Paleoalgology'* (pp. 226–236). Springer.

Taberner, M., & Bosence, D. (1995). An Eocene biodetrital mud-mound from the Southern Pyrenean Foreland Basin, Spain: An ancient analogue for Florida Bay Mounds? In *Carbonate mud-mounds: their origin and evolution* (Vol. 1, pp. 421–437).

Tapley, B., Ries, J., Bettadpur, S., Chambers, D., Cheng, M., Condi, F., & Poole, S. (2007). The GGM03 mean Earth gravity model from GRACE. in 'AGU Fall Meeting Abstracts'.

Tarboton, D. G. (1997). A new method for the determination of flow directions and upslope areas in grid digital elevation models. *Water Resources Research*, *33*(2), 309–319.

Vacherat, A., Bonnet, S., & Mouthereau, F. (2018). Drainage reorganization and divide migration induced by the excavation of the Ebro Basin (NE Spain). *Earth Surface Dynamics*, *6*(2), 369.

Vázquez, M., Jabaloy, A., Barbero, L., & Stuart, F. M. (2011). Deciphering tectonic-and erosion-driven exhumation of the Nevado–Filábride complex (Betic Cordillera, Southern Spain) by low temperature thermochronology. *Terra Nova*, *23*(4), 257–263.

Vennin, E., Rouchy, J.-M., Chaix, C., Blanc-Valleron, M.-M., Caruso, A., & Rommevau, V. (2004). Paleoecological constraints on reef-coral morphologies in the Tortonian–early Messinian of the Lorca basin, SE Spain. *Palaeogeography, Palaeoclimatology, Palaeoecology*, *213*(1), 163–185.

Vera-Peláez, J. L., Lozano-Francisco, M. C., Fernández, J. R., & Sánchez, M. C. (2004). Molluscos del Tirreniense (Pleistoceno Superior) de la playa la Araña-Cala del Moral (Málaga). *Revista Española de Paleontología*, *19*(2), 260–262.

Vergés, J., Millán, H., Roca, E., Muñoz, J., Marzo, M., Cirés, J., et al. (1995). Eastern Pyrenees and related foreland basins: Pre-, syn- and post-collisional crustal-scale cross-sections. *Marine and Petroleum Geology*, *12*(8), 903–915.

Vissers, R., Platt, J., & Van der Wal, D. (1995). Late orogenic extension of the Betic Cordillera and the Alboran domain: A lithospheric view. *Tectonics*, *14*(4), 786–803.

Viveen, W., Schoorl, J., Veldkamp, A., Van Balen, R., Desprat, S., & Vidal-Romani, J. (2013). Reconstructing the interacting effects of base level, climate, and tectonic uplift in the lower Miño river terrace record: A gradient modelling evaluation. *Geomorphology*, *186*, 96–118.

Whipple, K. X., & Tucker, G. E. (1999). Dynamics of the stream-power river incision model: Implications for height limits of mountain ranges, landscape response timescales, and research needs. *Journal of Geophysical Research*, *104*(B8), 17,661–17,674.

Whittaker, A. C., & Boulton, S. J. (2012). Tectonic and climatic controls on knickpoint retreat rates and landscape response times. *Journal of Geophysical Research*, *117*, F02024. https://doi.org/10.1029/2011JF002157

Whittaker, A. C., Cowie, P. A., Attal, M., Tucker, G. E., & Roberts, G. P. (2007). Contrasting transient and steady-state rivers crossing active normal faults: New field observations from the Central Apennines, Italy. *Basin Research*, *19*(4), 529–556.

Wiedmann, J. (1960). Zur systematik jungmesozoischer Nautiliden unter besonderer berücksichtigung der iberischen Nautilinae d'orb. *Palaeontographica Abteilung A*, *1*, 144–206.

Willett, S. D., McCoy, S. W., Perron, J. T., Goren, L., & Chen, C.-Y. (2014). Dynamic reorganization of river basins. *Science*, *343*(6175), 1248765.

Wilson, J., Roberts, G., Hoggard, M., & White, N. (2014). Cenozoic epeirogeny of the Arabian Peninsula from drainage modeling. *Geochemistry, Geophysics, Geosystems*, *15*, 3723–3761. https://doi.org/10.1002/2014GC005283

Zazo, C., Goy, J. L., Dabrio, C. J., Bardaji, T., Hillaire-Marcel, C., Ghaleb, B., et al. (2003). Pleistocene raised marine terraces of the Spanish Mediterranean and Atlantic coasts: Records of coastal uplift, sea-level highstands and climate changes. *Marine Geology*, *194*(1), 103–133.

Zazo, C., Silva, P., Goy, J., Hillaire-Marcel, C., Ghaleb, B., Lario, J., et al. (1999). Coastal uplift in continental collision plate boundaries: Data from the Last Interglacial marine terrace of the Gibraltar Strait area (south Spain). *Tectonophysics*, *301*(1), 95–109.

Zeck, H. P., Monié, P., Villa, I., & Hansen, B. (1992). Very high rates of cooling and uplift in the Alpine belt of the Betic Cordilleras, Southern Spain. *Geology*, *20*(1), 79–82.